Recursive partitioning and Gaussian Process Regression for the detection and localization of damages in pultruded Glass Fiber Reinforced Polymer material

Received: 2 September 2020 | Revised: 24 May 2021 | Accepted: 25 May 2021

DOI: 10.1002/stc.2805

RESEARCH ARTICLE

WILEY

Recursive partitioning and Gaussian Process Regression for the detection and localization of damages in pultruded Glass Fiber Reinforced Polymer material

Giosuè Boscato[1] | **Marco Civera**[2,3] | **Luca Zanotti Fragonara**[3]

[1]Laboratory of Strength of Materials, IUAV University of Venice, Venice, Italy

[2]Department of Mechanical and Aerospace Engineering, Politecnico di Torino, Torino, Italy

[3]School of Aerospace, Transport and Manufacturing, Cranfield University, Cranfield, UK

Correspondence
Luca Zanotti Fragonara PhD, School of Aerospace, Transport and Manufacturing, Cranfield University, Cranfield, UK.
Email: l.zanottifragonara@cranfield.ac.uk

Summary

In this paper, a methodology for the detection and localization of damages in composite pultruded members is proposed. This is particularly relevant to thin-walled pultruded members, which are typically characterized by orthotropic behavior, anisotropic along the fibers and isotropic in the cross section. Hence, a method to detect and localize damage, and the influence these might have on the performance of thin-walled Glass Fiber Reinforced Polymer (GFRP) members, is proposed and applied to both numerical and experimental data. Specifically, the numerical and experimental modal shapes of a narrow flange pultruded profile are analyzed. The reliability of the proposed semiparametric statistical method, which is based on Gaussian Processes Regression and Bayesian-based Recursive Partitioning, is analyzed on a narrow flange profile, artificially affected by sawed notches with incremental depth. The numerical investigation is carried out via finite element models (FEMs) of the cracked beam, where the dynamic parameters and the modal shapes are computed. In total, three different crack sizes are investigated, to compare the results with the experimental ones. Finally, the proposed approach is further extended and validated on numerically simulated frame structures.

KEYWORDS

Bayesian-based recursive partitioning, damage identification, FEM, Gaussian processes, modal analysis, pultruded GFRP material

1 | INTRODUCTION

Materials such as the Fiber Reinforced Polymer (FRP) are widely used in most engineering fields such as automotive, aerospace, or constructions. Their main characteristics are the high strength and stiffness related to the volumetric mass. Generally, their performances are favorable with respect to other more traditional materials for what concerns the corrosion resistance, the low thermal expansion coefficient, and the enhanced fatigue life.[1]

The mechanical response of FRP structural members are characterized by elastic-brittle behavior, remaining linear even for large values of strains. The collapse mechanisms are affected by the material crushing and stability, and the global

failure is typically induced by local fiber buckling and/or resin breakage. These members come typically as thin-walled, manufactured via a pultrusion process.[2,3] This manufacturing process defines the mechanical behavior of the composite material, which is made of fibers that follow the main axis of the profile and hence the direction of the pultrusion process and resin to join the fibers and define the shape. This makes the pultruded material anisotropic along the fibers and isotropic transversally, through a layered structure constituted by unidirectional rovings and continuous mats.

In general, common non-destructive inspection techniques (NDT)—such as ultrasonic, thermography, and radiography—are used for the local detection of defects and small cracks; thus, these local methods do not allow quick assessment nor the global estimation of the structure. On the other hand, vibration-based methods are directly related to the structural response and performance[4,5] and can be used to extrapolate both global and local damage-related information; their usefulness lies also in being easy appliable to different structural fields ranging from aerospace to masonry buildings (see, e.g., Ferraris et al. and Civera et al.[6,7]). In this context, some authors proposed the change in natural frequencies[8,9] as a damage indicator. Other approaches are focusing on the difference of curvature in the mode shapes to locate damage through the Modal Curvature Method (MCM).[10,11] These two categories are better known as frequency-based (FB) and modeshape-based (MB) damage detection.[12] Derivation of these latter methods has been proposed by processing further the curvature mode shape data through the Gapped Smoothing Method (GSM),[13] Global Fitting Method (GFM),[14] and the Curvature Operating Shape.[15] These latter procedures are based on the spatial derivatives of the experimental modal shapes that tend to amplify the measurement noise. Indeed, techniques based on multiple output channels and mode shapes are generally the most accurate way to perform damage localization, even if techniques based on acquisitions at a single point have been proposed (e.g., Civera et al.[16]).

The method presented here is an example of an MB approach. To avoid the numerical differentiation step,[17] an approach based on Gaussian Process (GP) regression[18] is proposed in this paper to assess the structural condition of a complex structure material characterized by orthotropic behavior such as pultruded GFRP beams. An evolution of GP is applied through the Treed Gaussian Process (TGP) approach,[19,20] which works by partitioning the function space into regions covered by distinguished GP with distinct covariance functions.

The efficacy of TGP has been verified through the damage assessment of narrow flange GFRP pultruded profile. This has been firstly investigated on a simply supported beam, for which experimental data were available from laboratory tests, and then for two-dimensional frame structures.

The remaining of this paper is organized as follows. In Section 2, the theoretical background of the proposed methodology is recalled. In Section 3, the experimental case study of the GFRP beam is described. The results are discussed in Section 4, also comparing the TGP outcomes with the ones obtained from more established techniques. Finally, Section 5 discusses the extension of the concept to two-dimensional frame structures. The paper ends with Section 6.

2 | DAMAGE DETECTION AND LOCALIZATION USING TGPS

An algorithm based on Bayesian Classification and Regression Trees (CARTs) combined with GP regression is here investigated as a mean for the detection of discontinuities in the mode shapes.

The so-called TGP regression, also known as Gaussian Process Regression Trees, were proposed as a mean to deal with time- and/or space-dependent heteroskedastic data in a principled manner.[19] For structural purposes, they have been used for sensitivity and uncertainty analyses of discontinuous responses of nonlinear models[21] and their data-driven system identification.[22] This method was also previously applied in the Structural Health Monitoring (SHM) context, specifically to the case study of the Tamar and Z24 bridges, using their natural frequencies as a time-dependent feature[23,24] but not spatially on mode shapes. A simplified algorithm was also presented in Zhang et al.[25,26] TGPs were also validated for the identification of manufacturing imperfections in Civera et al.[27] These are here proposed as an automatic tool for damage localization in the case of multiple notches. Some preliminary results, applied on a very simplified finite element (FE) model with 1D beam element, were reported in Civera et al.[28] The procedure has been here further refinished and validated on a more complicated numerical model, as well as tested on experimental data for damage detection and localization.

An abundance of similar approaches exists. For instance, the kernel-based algorithm proposed by Corrado et al.[29] allowed a spatial switch point in the GP covariance, which different characteristics near a point and on either side of the point, to localize pointwise discontinuities. Gauthier et al.[30] applied a higher-order derivative discontinuity (HODD) approach for the same purpose. Several approaches for damage localization have been also proposed in recent years by Casciati and Elia,[31] An et al.,[32] and Stojić et al.[33]

An in-depth description of the theoretical background of Gaussian Process Regression and Bayesian Trees is omitted as it is beyond the scope of this article. The reader can refer to the works of Gramacy and Lee[20] for a complete dissertation. In brief, the TGP process can be summarized as fitting piece-wise low-order regression GP models $f(\bar{x})$ on the independent variable $\bar{x}$ space, which is the one-dimensional main axis of the beam in our case. The procedure is a Markov chain Monte Carlo (MCMC) "random walk"; thus, the acceptance criterion is crucial to validate or abort the new walked-in tree state at the generic ith step. In particular, the process requires the Metropolis–Hastings ratio, defined by the posterior log-probability of the attempted tree over the one from the current tree, inherited from the previous step, to be inferior to a uniformly sampled random value between [0,1].

Each distinct GP has its own, fixed covariance function and is therefore fitted only over a well-defined spatial region. Hence, switching points between contiguous GPs would ideally coincide with punctual singularities, leading to the detection and localization of discontinuities. Indeed, the use of simple GP on the modal response requires the beam to be uniform or at least smooth; for a structure with no geometrical or material discontinuities, this assumption is valid only for an undamaged (UD) beam.

The TGP procedure is summarized in Figure 1. Four jumping criteria in the Markov space—Grow, Prune, Change, and Rotate—were used, defined accordingly to Chipman et al.[34] A Gibbs sampling scheme[35] was used for the Bayesian inference of the updated parameters.

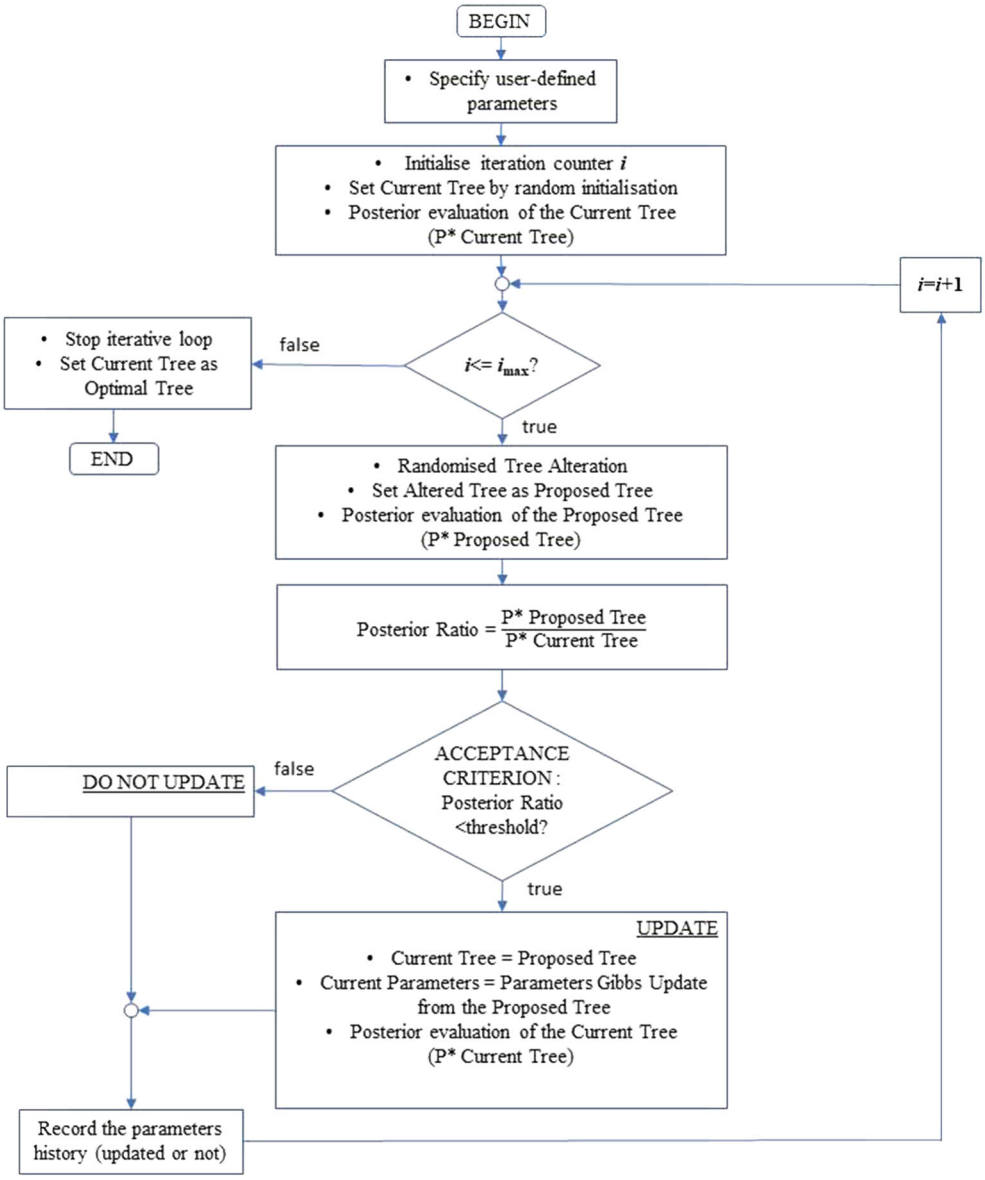

FIGURE 1 Illustrative flowchart of the Treed Gaussian Process algorithm[27]

2.1 | Methodology: The TGP algorithm

A script coded in R was used here, implementing the package for TGP as proposed by Gramacy.[36] Specifically, the TGP with jumps to Limiting Linear Model function was used, to benefit from any potential speedup in the uninteresting part of the input space (i.e., in any region with zero or close to zero response).[20] Major technical details can be found in Civera et al.[27] An Active Learning-Cohn algorithm (ACL)[20] was used to maximize the expected information design, through the sequential design of experiments (sequential DoE). This works by calculating the $\Delta\sigma^2(\bar{x})$ statistics for any $\bar{x}$ in the predictive locations and then selecting the locations with the highest standard deviation in predictive output. The proper definition, plus all the due details, can be found in previous studies.[37,38] The obtained statistics were then used to compute the expected improvement (EI), in terms of differences in predictive output quantiles[39] for each predictive location, according to the global minimum.[40] Search locations were also pre-sorted to further improve the algorithm capabilities.[41]

A burn-in period of 2000 samples was fixed to ensure a stationary chain. The statistics were then established over further 5000 rounds, for a total of 7000, with two restarts. This was done in accordance with the recommendations of Chipman et al.[42] to restart the Markov chain at least once to better explore the marginal posterior for the maximum a posteriori (MAP) trees $\hat{T}$, by taking into account only the most fitted repetition. To improve the MCMC performance, the process was initialized with an additional run of a Bayesian treed linear model.[42] This implies a pre-split of the input space using Chipman's linear model, that is to say, a linear burn-in. At each run, $\hat{T}$ and the corresponding parameters $\hat{\theta} \mid \hat{T}$ are stored, being the switching points located at the branches.

2.2 | Treed partitioning example

For the reader's convenience, an example of TGP partitioning is reported in Figure 2. The specific case is the application of TGP partitioning to the sixth mode shape of a 1-D linear elastic FE model of a 1-m-long cantilever beam model, with the Euler–Bernoulli beam model and damage modeled as stiffness-reduced elements.[43] Specifically, a 40% reduction of Young's modulus was inserted at 28 cm from the clamped end. For statistical validation, the code has been re-run 1000 times. In this example, the TGP branched only 78 times out of 1000, always producing only one partition (i.e., a one-branch tree). Figure 2a shows an example of one TGP partition. To the left, the inferred mode shape is plotted superimposed to the training data; the dashed line highlights the branching point at the boundary between subsequent GPs. To the right, the corresponding regression tree is sketched. The branching criterion is colored accordingly to its corresponding dashed line. The position of the branching points for the 1000 re-runs of the code is depicted in Figure 2b with the resulting probability density function (pdf). The mean value of the pdf stands at 0.2727 m.

In other numerical data, and in the experimental ones as well, it was observed that the TGP partitioning algorithm tends to overfit the provided training set, resulting often in an excessively large number of branches. The assumption made at this point was to consider a single point source of impending damage. Nevertheless, the fraction of one-branch trees over the total was always inexistent or negligible; considering the research limited to them would have been neither statistically valid nor practically sensed. Hence, hereinafter, all experimental results and pdfs are referred to the first partition only, independently of the actual number of branches. This is based on the assumption that the first partition is supposed to be the most discriminative in a classification tree. It was found both in numerical simulations and experimental data that the first branches clustered very well around specific areas of the beam.

3 | CASE STUDY

3.1 | Description of the GFRP pultruded profiles

Reinforced composite materials can be made with several different production techniques, each one characterized by its own advantages and limitations. In the pultrusion processing method, the continuous E-Glass fiber reinforcement (layers of unidirectional rovings and continuous mats) is impregnated with a thermoset resin-based matrix and pulled through a heated die that provides the cross-sectional shape of the profile. The pultrusion technology, and the related FRP pultruded shapes themselves, are widely explained by the American pultruders' Design Manuals[2,3,44,45] and the Eurocode.[46]

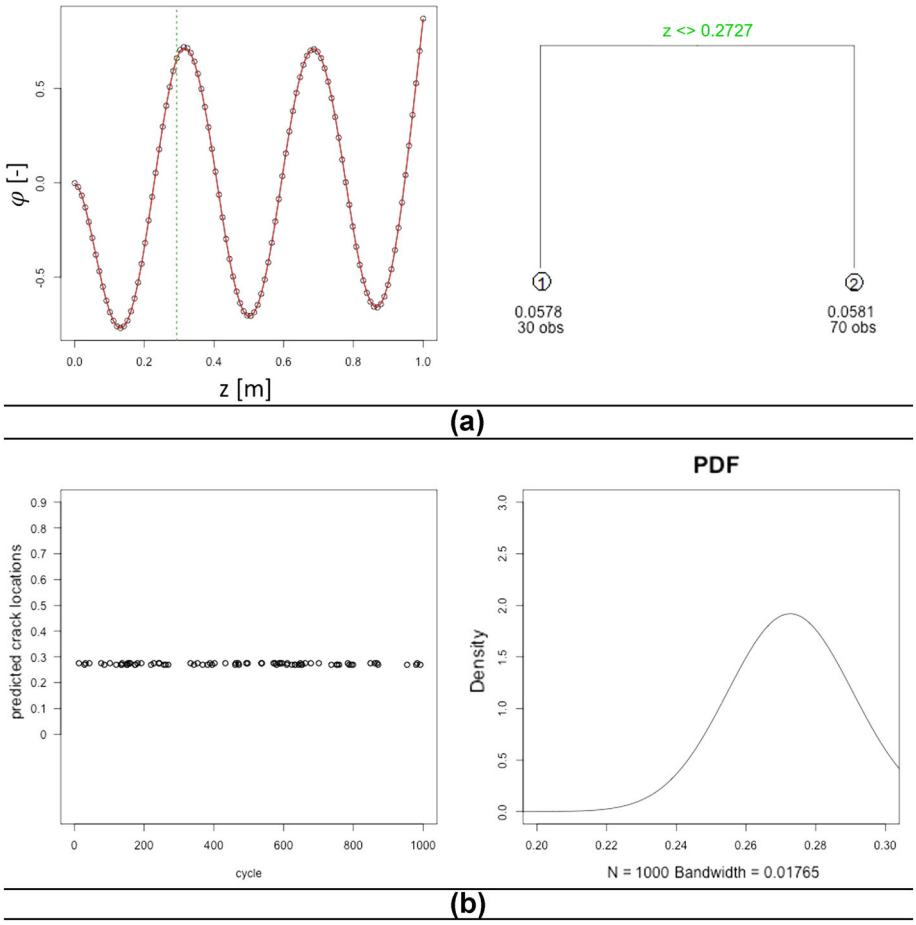

FIGURE 2 (a) Left: TGP regressions (solid red lines) over numerical data (black circles). Right: the corresponding hierarchical dendrogram of GP fittings. (b) Left: plot of all localizations along 1000 re-runs of the code; right: corresponding probability density function

The pultruded GFRP elements investigated feature a volume percentage for matrix (Vinilester 980-35) and fiber (E-Glass) of 60% and 40%, respectively.

Table 1 lists the mechanical properties of the studied profile, quantified using tests carried out according to ASTM standards for plastic samples and UNI EN 13706[47] for full-scale pultruded profiles.

Standard pultruded FRP are thin-walled profiles with several cross-section shapes (narrow flanges, wide flanges, circular, and square cross sections).

The pultruded GFRP material is investigated in this paper through an open thin-walled cross section. An open narrow flanges cross-section profile with simply supported boundary condition is experimentally investigated here considering the maximum (Jmax) moment of inertia corresponding with the accelerometer positions along the y axis.

The pultruded beam was made by continuous E-Glass fiber reinforcement, layers of unidirectional rovings and continuous mats (embedded in a thermoset resin-based matrix) that are generally schematized by laminated configuration, external mat (triaxial layers $\pm 45^\circ$ and 0°) and internal unidirectional roving (0°) layer.[1]

The profile analyzed in this paper refers to the coordinate system defined by the x-y plan of cross section and z axis normal to it (Figure 3). Fibers run along the global z axis of each element exhibiting orthotropic behavior, that is, anisotropic in the z direction and isotropic in the x and y directions.

The characteristics of the analyzed composite pultruded element are reported in Table 2; in addition to the physic and geometric properties, the table shows the second moment of area J, torsional constant J_t, length L, and the relationship between the length and the cross-section height (L/h) of every profile. The slenderness ratios (λ) were obtained from $\lambda = L/\sqrt{(J/A)}$, while (t/L_w) shows the relationship between the thickness t and the plate's length L_w.

TABLE 1 Mechanical and physical characteristics of pultruded material extracted by specimens' pultruded profile

Properties	Test method	Notation	Mean value
Longitudinal tensile modulus of elasticity	ASTM D638	$E_z = E_L$	28.5 (GPa)
Transverse tensile modulus of elasticity	ASTM D638	$E_y = E_x = E_T$	8.5 (Gpa)
Transverse shear modulus of elasticity	EN 13706 (full scale)	$G_{yx} = G_L$	3.5 (Gpa)
In-plane shear modulus of elasticity		$G_{xz} = G_{yz} = G_T$	2.5 (Mpa)
Longitudinal Poisson's ratio	ASTM D3039	$\nu_{zx} = \nu_{zy} = \nu_L$	0.25
Transversal Poisson's ratio	ASTM D3039	$\nu_{xy} = \nu_{yx} = \nu_T$	0.12
Longitudinal tensile strength	ASTM D638	$\sigma_{zt} = \sigma_{Lt}$	350 (Mpa)
Transverse tensile strength	ASTM D638	$\sigma_{xt} = \sigma_{yt} = \sigma_{Tt}$	70 (Mpa)
Longitudinal compressive strength	ASTM D695	$\sigma_{zc} = \sigma_{Lc}$	413 (Mpa)
Transverse compressive strength	ASTM D695	$\sigma_{xc} = \sigma_{yc} = \sigma_{Tc}$	80 (Mpa)
Shear strength	ASTM D2344	$\tau_{xy} = \tau_{xz} = \tau_{yz}$	40 (Mpa)
Density	ASTM D792	Γ	1734 kg/m^3
Fibers percentage	ASTM D2584	V_f	45%

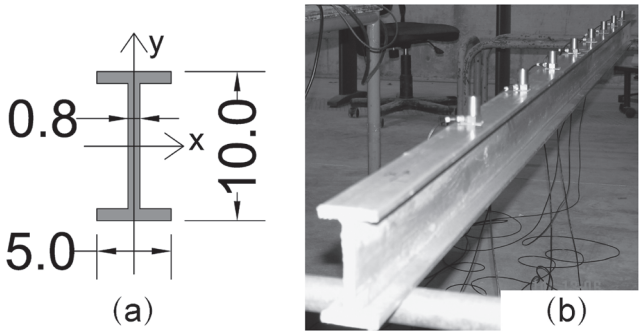

FIGURE 3 Narrow flanges NF profile, geometrical details for the cross-sectional shape (a) (dimensions in centimeters) and photo along the *y* axis (b)

TABLE 2 Geometrical and physical properties of the pultruded beam's profile

Profile	J (cm^4)	J_t (cm^4)	L (cm)	*Area* (cm^2)	L/h	λ	t/L_w	*Weight* (kg)	*Density* (kg/m^3)
"NF," $J_{\min}$	17.02	3.14	300	14.72	30	139.5	0.0026	7.62	1727
"NF," $J_{\max}$	209.22				15	39.8			

3.2 | Test setup and experimental modal analysis

Regarding the test setup, Figure 4a,b shows the cross section of the configuration studied, the scheme of the accelerometers (A0, A1, ..., An) and excitation positions (B0, B1, ..., Bn) considering a gap between accelerometer and excitation points by 322 mm. Twelve accelerometers were used for nine excitation points for UD beam, whereas for damaged configurations, B4 excitation point was used. The damage was simulated by sawing a notch into the beam at a fixed cross section, localized at 532 mm from the right end (Figure 4b); the incremental damage was achieved by increasing the cut's depth, similarly to other recent works[48] details are shown in Figure 4c. The simply supported condition was achieved by positioning the beam on cylindrical elements.

The excitation pulse of the structural element has been generated by a Dytran 5850A instrumented hammer with a specifically calibrated tip stiffness to obtain complete broad oscillation periods. Accelerometers BBN model 507Lf with a mass of 10 g and a frequency range of 0.1 and 5–12 kHz were used. Both the hammer and the sensors are piezoelectric sensing elements featuring a cylindrical shear stress configuration with an integral charge preamplifier and are

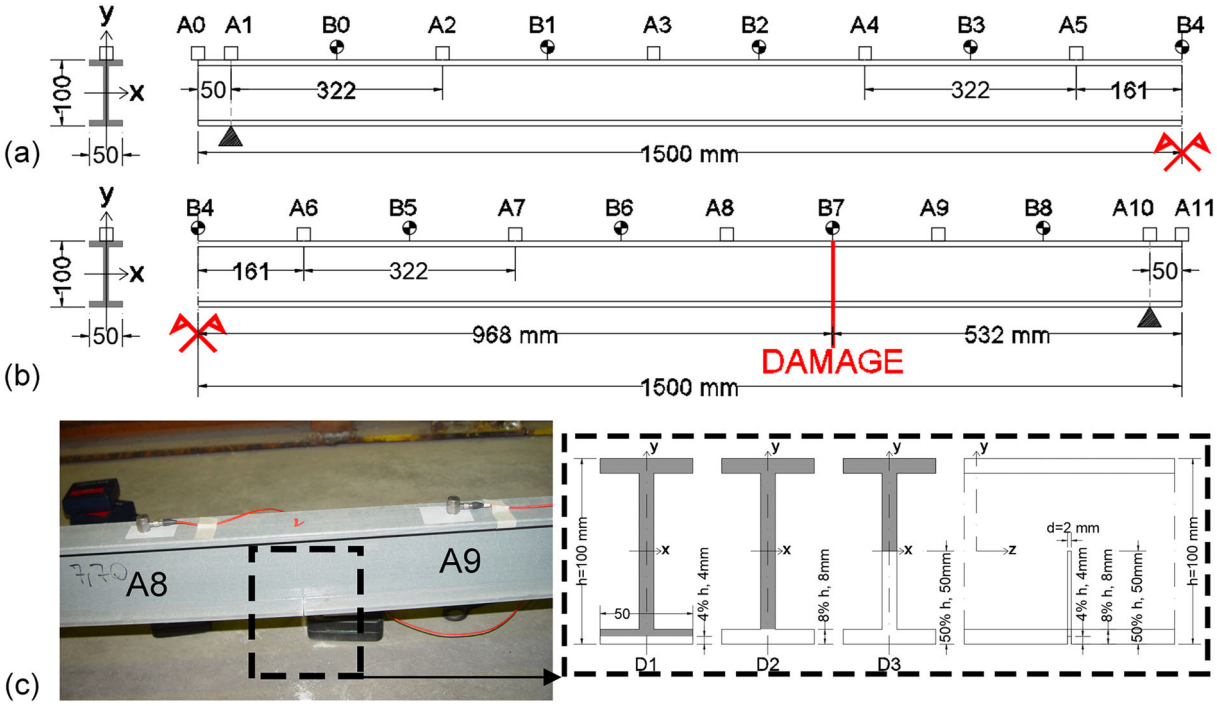

FIGURE 4 Undamaged half-beam and sensor layout (a), damaged half-beam and sensor layout (b), and damage details (c)

connected to a data acquisition system. The acquisition phase has been synchronized with the trigger pulse originated by the instrumented hammer. A post-processing scheme was applied to all signals: a digital band-pass filter was applied to eliminate frequencies below 1 Hz and above 150 Hz.

Figure 5 represents the stabilization diagrams for one set of acquired data for UD and damaged (D1, D2, and D3) configurations. The algorithm used for identification was the Eigensystem Realization Algorithm (ERA)[49] as the response available were free-decay responses. The stabilization diagrams show the stable modes as filled circles, according to a few simple stabilization criteria such as: maximum frequency variation 1%; maximum damping variation 10%; minimum Modal Assurance Criterion (MAC)[50]: 0.98. Furthermore, poles with negative damping or with damping higher than 10% were discarded as physically unrealistic.

Table 3 summarizes the results of the identification process across all different signals. Frequencies f and damping have been averaged after the modes have been clustered and matched based on the MAC value (>0.95).

Figure 6 summarizes the dynamic model and the different modal shapes for each impact on the UD profile.

3.3 | Numerical modal analysis

The numerical FE models were developed using ANSYS® Mechanical APDL™. About 30,000 nodes and 5000 SOLID186 elements were used to model the web and the flanges. The material was assumed as orthotropic; the set parameters—elastic moduli, Poisson's ratios, shear moduli, and density for all directions—are the experimentally defined ones enlisted in Table 1. The cross section of the pultruded profile is characterized by a random microstructure; therefore, the FE model of pultruded composite material is based on the homogenization procedure of fictitious periodic microstructure through three-dimensional representative volume element (RVE).[51,52] The right-handed reference system $\{O, x, y, z\}$ was set on the centroid of the left end of the beam, with the z axis parallel to the longitudinal direction ($Ez = \mathrm{EL}$), the y axis parallel to the GFRP cross-section direction of minimum moment of inertia $J_{\min}$, and the x axis parallel to the cross-section direction of maximal one $J_{\max}$. The structure was modeled as a simply supported beam. Hinges were located at the point of support over the metal bars; thus, two small cantilevered ends resulted, protruding 50 mm over. Considering only the 2.9-m-long tract included in between the two supports, 144 equally spaced locations were selected as output channels. The nodes were selected to be as close as possible to the reference line used for

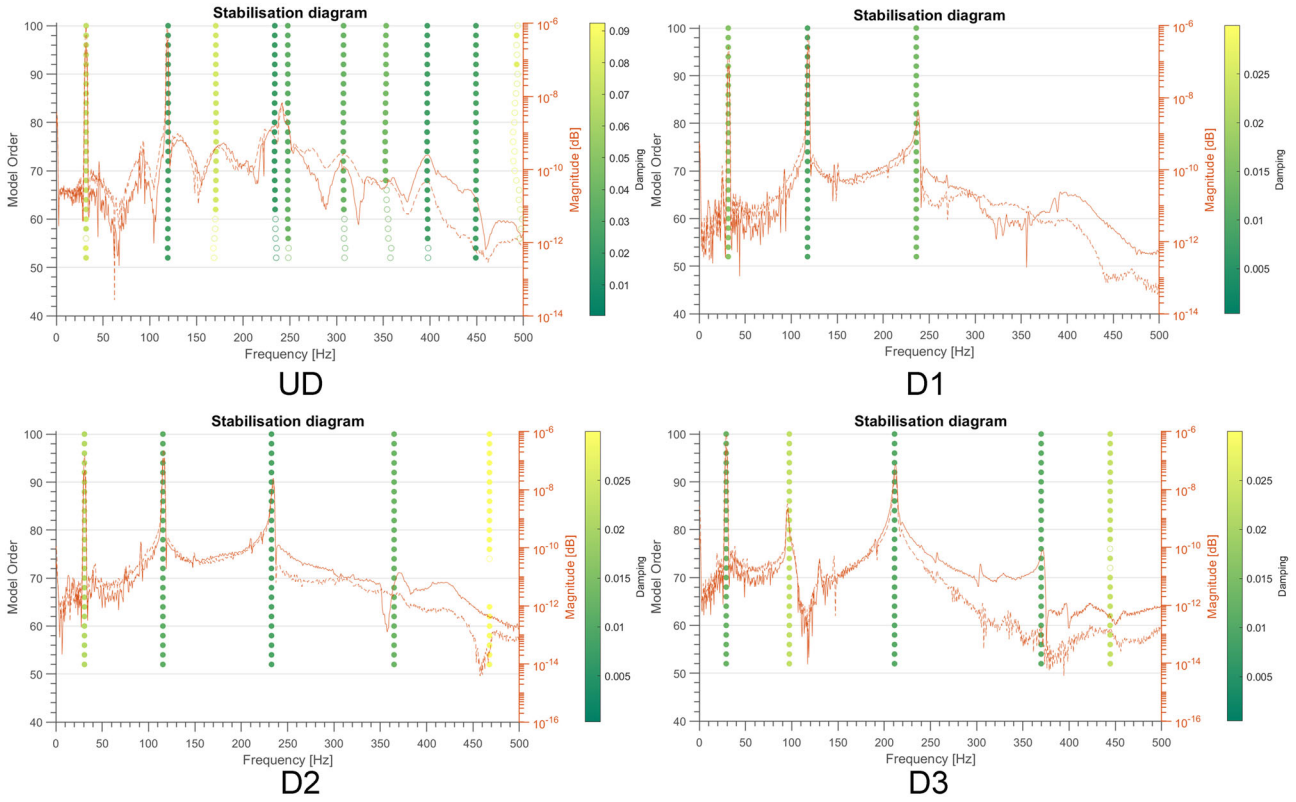

FIGURE 5 Stabilization diagrams using the B4 excitation position for undamaged (UD) and damaged (D1, D2, and D3) configurations

TABLE 3 Experimental modal analysis results

	UD		D1		D2		D3	
Modal shapes	***f*** **(Hz)**	**Damp**	***f*** **(Hz)**	**Damp**	***f*** **(Hz)**	**Damp**	***f*** **(Hz)**	**Damp**
Mode 1	31.9	5.3%	31.59	1.61%	30.83	2.14%	29.07	1.28%
Mode 2	119.7	1.95%	117.72	0.97%	115.46	1.12%	97.34	2.29%
Mode 3	247.8	1.35%	235.88	1.42%	232.57	0.93%	211.14	1.07%

placement of the physically-attached sensors in the experimental acquisitions—that is, the web and the upward flange mid-lengths.

Three finite element models (FEMs) were created, representing the structure damaged with a saw cut, modeled by removing some of the elements, considering three depths identical to the experimental case study depicted in Figure 4. This more realistic model was preferred over the classic approach of decreasing the element stiffness at the damage location, as it also allows to capture the potential nonlinear effects of breathing cracks.[16,53,54] The UD FE Model is depicted in Figure 7a; a zoom on the first damage level (D1) is reported in Figure 7b.

4 | RESULTS

4.1 | TGP applied to numerical mode shapes

Considering the four damaged mode shapes investigated for the numerical example (depicted in Figure 8), four levels of white Gaussian noise were artificially added to investigate the robustness of the TGP algorithm to noise. Specifically, four noise standard deviations, equal to $\sigma_n = 0.001$, 0.002, 0.005, and 0.01, were applied for any level of damage.

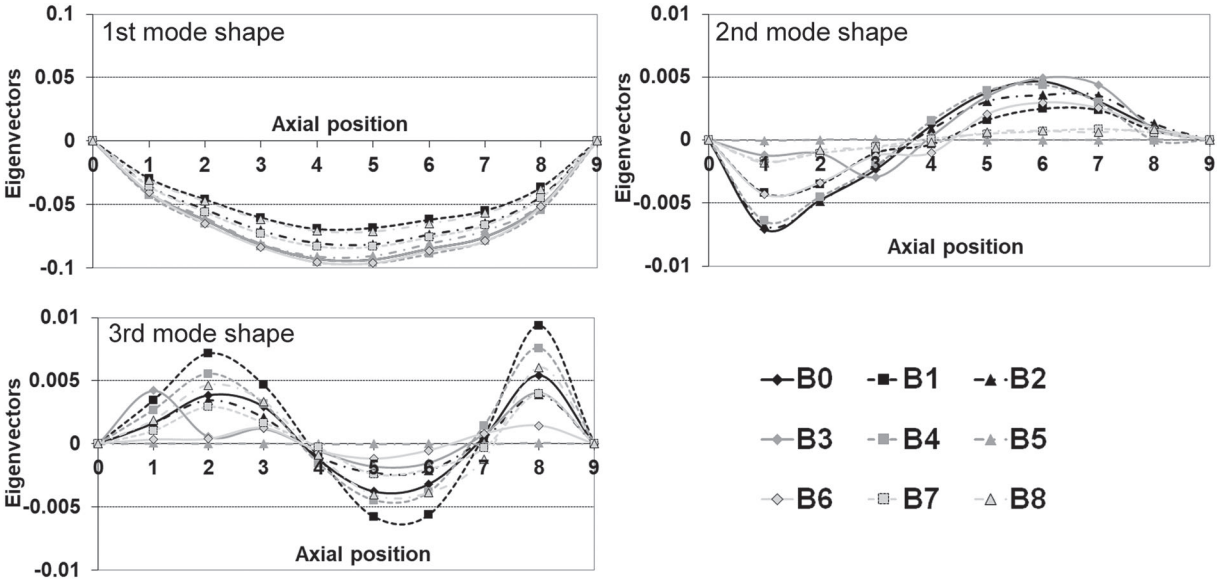

FIGURE 6 Experimental mode shapes, UD profile

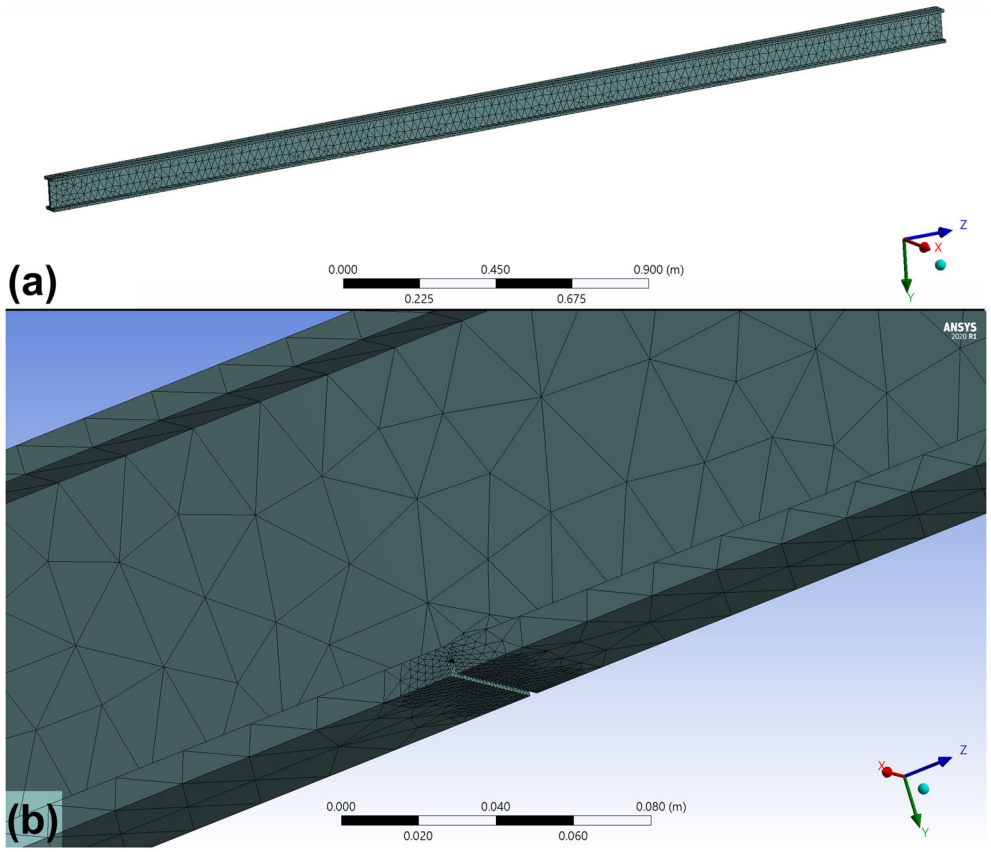

FIGURE 7 (a) The pristine beam and (b) the modeled saw cut. Three depths were considered, corresponding to D1, D2, and D3

Any of the 144 output channels was set as a possible candidate for damage localization. To investigate the influence on the performance due to the number of the sensors, five options were considered: with all nodes (144) activated, or only considering 72, 36, 18, or 9 output channels (always equally spaced).

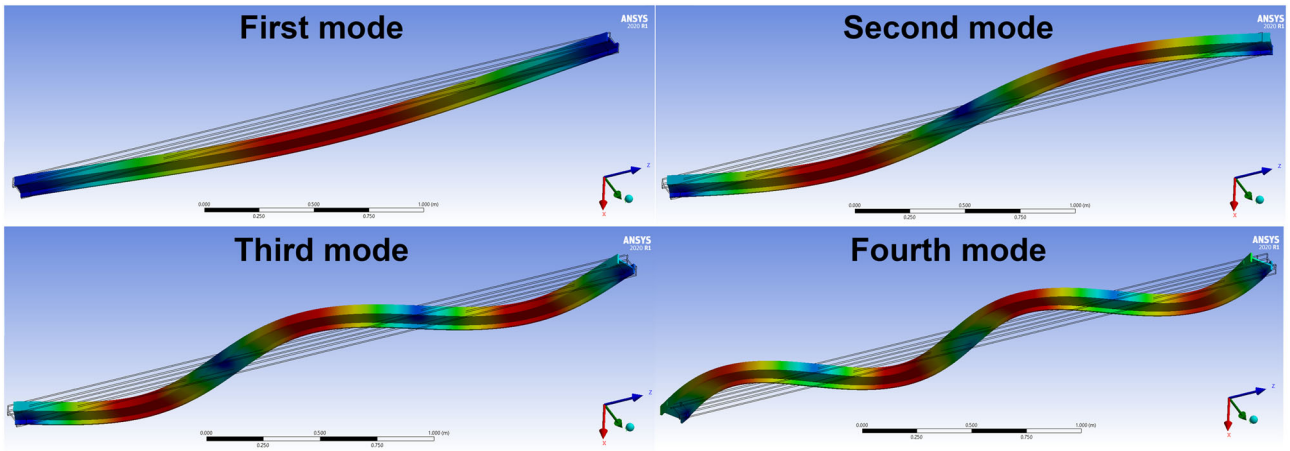

FIGURE 8 The undamaged beam mode shapes

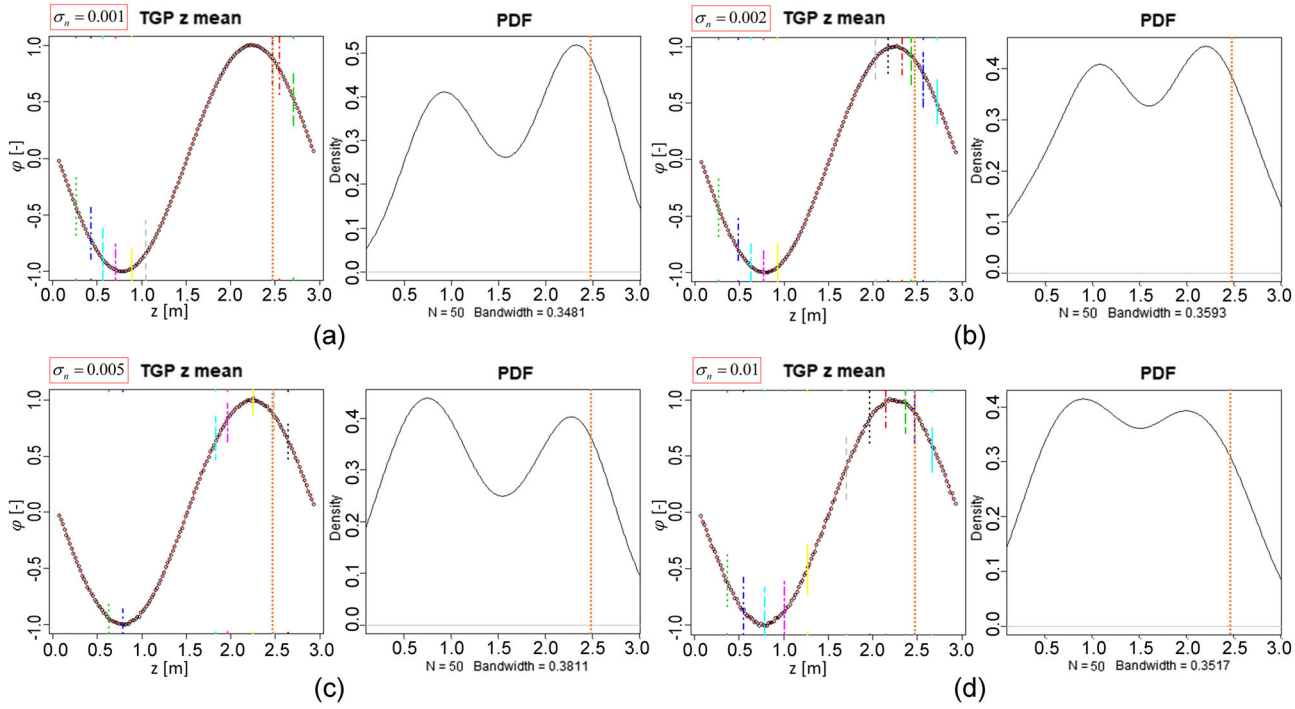

FIGURE 9 Damage Scenario D1 (extension: 4 mm), second mode shape, 144 channels. From (a) to (d): $\sigma_n = 0.001$, 0.002, 0.005, and 0.01. The dotted orange line indicates the actual damage location

The TGP regression computational demand increase with the number of potential damage locations, which for simplicity have been considered at the same locations of the virtual sensors. To validate statistically the results, a total of 50 TGPs were computed for each case, by re-running the code.

Due to the large number of numerical cases simulated, only a selected few cases are reported here for discussion in Figures 9–14. Only output channels in the $J_{\max}$ direction were considered and results are always picked from the first run (out of 50).

All bifurcations have been reported for completeness, superimposed to the input data on the left; each tract of vertical line represents a switching point, separating two adjacent GP regressions. The corresponding pdf of the first branching are reported on the right. The dotted orange line indicates the actual damage location.

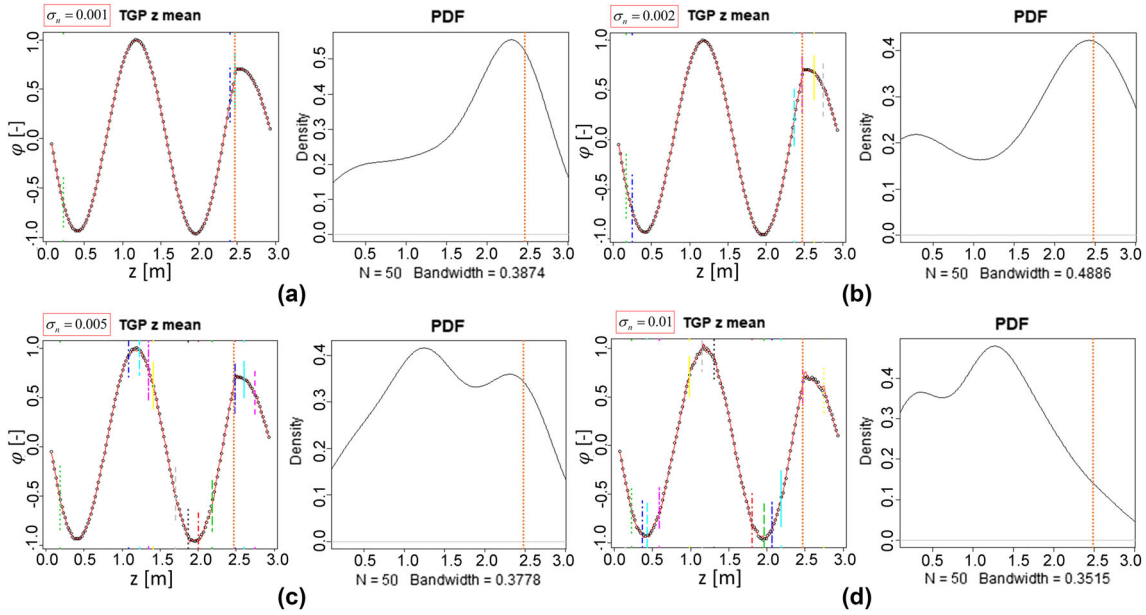

FIGURE 10 Damage Scenario D3 (extension: 50 mm), fourth mode shape, 144 channels. From (a) to (d): $\sigma_n = 0.001$, 0.002, 0.005, and 0.01. The dotted orange line indicates the actual damage location

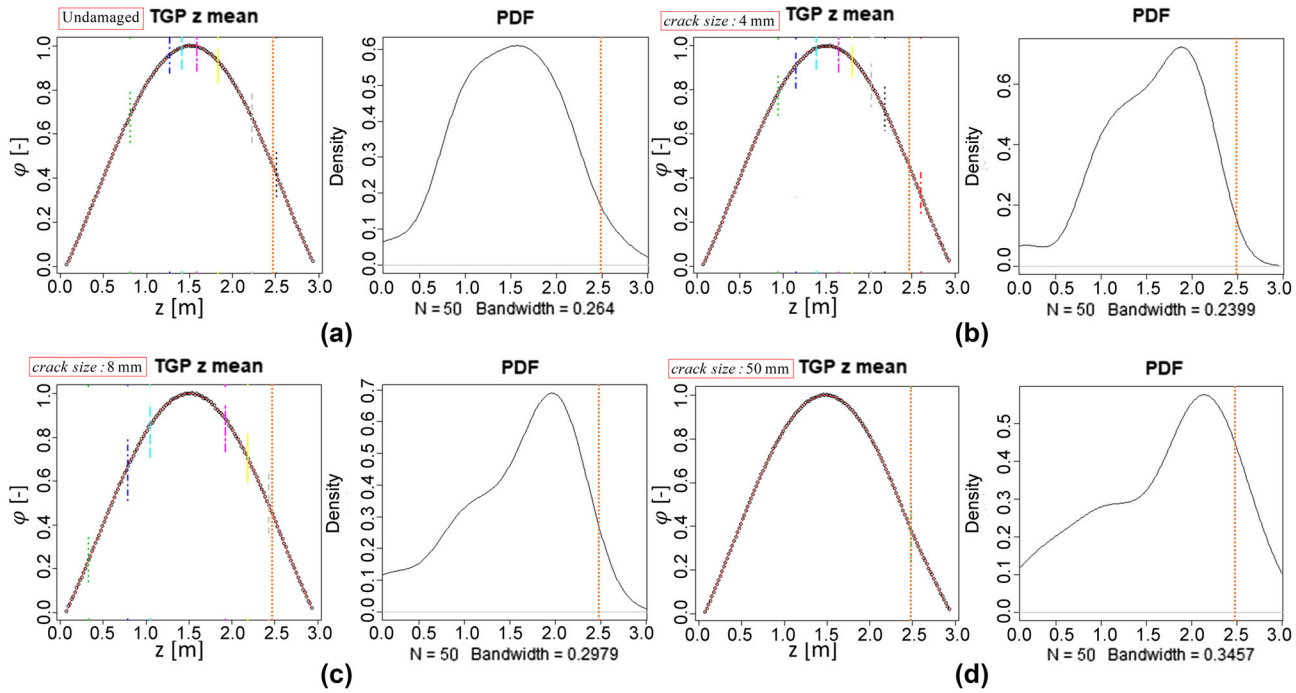

FIGURE 11 Noise equal to $\sigma_n = 0.001$, first mode shape, 144 channels. From (a) to (d): D0 (undamaged), D1, D2, and D3.The dotted orange line indicates the actual damage location

Figures 9 and 10 show, respectively, the consequences of noise. The first (D1, extension 4 mm) and last (D3 extension 50 mm) damage scenarios are considered for the second and fourth mode shapes, respectively. Figure 11 displays the effects of changing the damage size; the comparison is run over the minimum level of noise ($\sigma_n = 0.001$) for the first mode and the highest level of noise in this case ($\sigma_n = 0.01$) for the third mode (Figure 12).

It can be seen (Figure 9) how the form of the second eigenshape exalts the effects of the damage, which is located close to its second antinode. However, these effects cannot be easily distinguished from the tendency of the TGP to

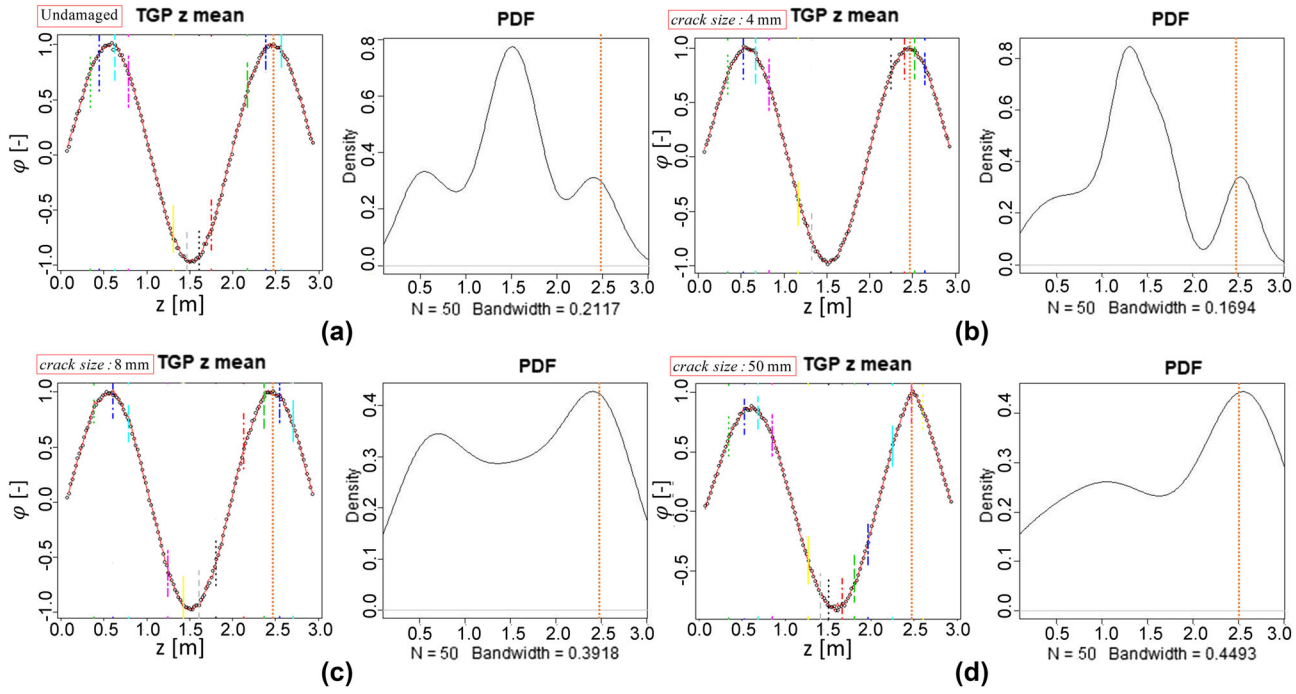

FIGURE 12 Noise equal to $\sigma_n = 0.01$, third mode shape, 144 channels. From (a) to (d): D0 (undamaged), D1, D2, and D3. The dotted orange line indicates the actual damage location

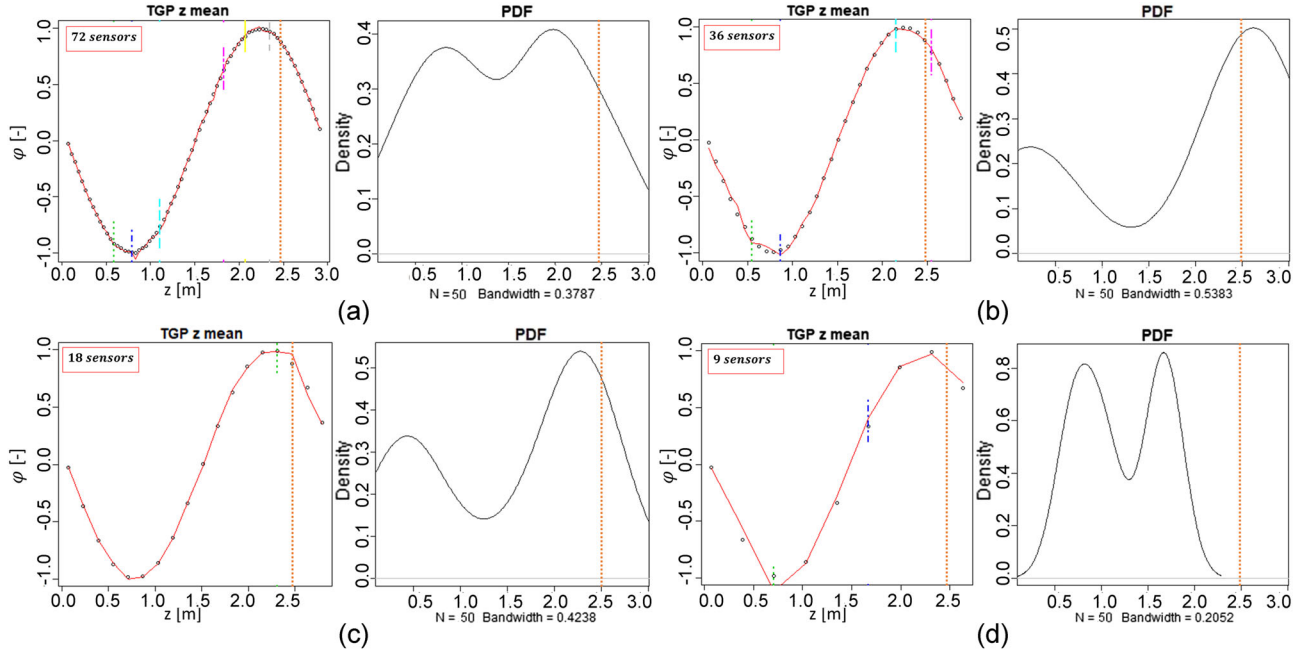

FIGURE 13 Damage Scenario D2 (extension: 8 mm), noise equal to $\sigma_n = 0.005$, second mode shape. From (a) to (d): 72, 36, 18, and 9 equally spaced output channels. The dotted orange line indicates the actual damage location

bifurcate at the other mode shapes' extreme point. That is to say, the first antinode, corresponding to a local minimum, is confused with damage-related discontinuities in the shape. This issue is intensified by the increasing noise level. As it will be better explained in the next sections, this problem can be addressed in practice by comparing more mode shapes at once.

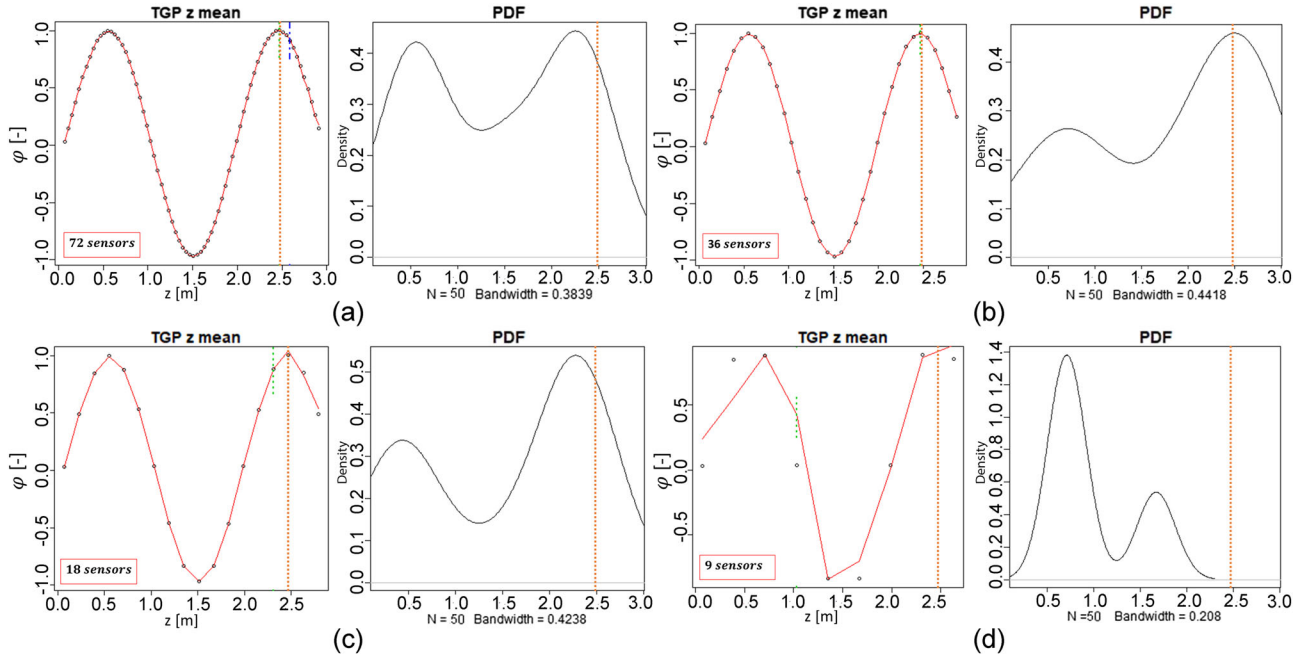

FIGURE 14 Damage Scenario D1 (extension: 4 mm), noise equal to $\sigma_n = 0.002$, third mode shape. From (a) to (d): 72, 36, 18, and 9 equally spaced output channels. The dotted orange line indicates the actual damage location

It has been noticed that, to a certain extent, increasing the noise reduces the number of partitions, as the surrogate model becomes less overfitted. However, when the signal-to-noise ratio overcomes a certain point, this trend reverses, and the model fits the noise with an unmanageable number of unneeded partitions. This can be due to a minimal optimum between less overfitting error on a more varied dataset and the more elaborate function to represent. Generally speaking, it was found that a slight increase of the noise level may cause the fourth mode (which has a more complex shape) to branch more times, while instead decrease the number of bifurcations for Modes #1, #2 and #3, which have overall "simpler" eigenshapes.

Out of all the modes investigated for this preliminary numerical study, the fourth mode shape was found to be the most affected by the presence of damage (Figure 10). From the numerical example reported, it is noticeable how increasing the noise over a certain amount causes the TGP model to bifurcate more at the antinodes, hiding the actual damage location.

The effects of damage size are very important as well, as can be inferred from Figure 11.

In the UD case, the model basically branches at random, with a noticeable preference for the beam midlength. This is most probably due both to the specific algorithm, which is likelier to bifurcate far from the edges and to the presence of the mode shape sole antinode.

The damage position becomes very evident when the size is enlarged. On the other hand, the saw cut is hardly visible in the first mode shape if further noise is added, independently from its depth; partitions of the first mode are overwhelmingly located in the mid-beam. For the largest amount of noise, the damage is instead quite easily captured by the third mode shape, as its location fall very close to one of its antinodes (Figure 12). It can be seen in Figure 12a how the algorithm, even without damage and with three identical antinodes, preferably branches at the center of the data array. This is altered by the insertion of damage, which does not only increase the probability of first partitioning at its location (as expected) but seems also to affect the probability distribution at other locations, making the first branch less likely to happen at the central antinode.

Finally, the influence of the number of sensors is portrayed in Figures 13 and 14 by fixing the other variables. The results for 144 sensors are omitted as they have been considered in all the other cases reported so far. It can be seen that reducing the number of the output channels up to only 18 sensors does not impact negatively on the damage localization procedure and can even reduce the overfitting, actually improving the readability of the results.

To sum up, it seems plausible to state that on numerical data, a certain (small, but not too small) amount of independent and identically distributed noise produced less overfitted regressions, thus less superfluous branches.

That means that the noise helps to stabilize the branching fitting on data, improving the final results (often, rather than a single, unique partition corresponding to the damage location, a "denser" area can be circumscribed, which envelopes the slot actual position). However, larger amounts of noise are disruptive, as expected. For what concerns the number of sensors, it was found that this is the most sensitive parameter, as it affects noticeably the computational effort required by the algorithm. Figure 15 reports the box plots of the time elapsed to run a single TGP regression, considering all the re-runs performed (with a non-optimized version of the code) on an Intel ® Core™ i7-7700HQ CPU with 2.80-GHz base frequency. The cases are numbered as follows: Cases 1–4 correspond (in the same order) to the four mode shapes of the UD beam with σ_n=0.001. Cases 5–8, 9–12, and 13–16 represent the same but with σ_n= 0.002, σ_n= 0.005, and σ_n= 0.010, respectively. The same order is repeated for D1 (Cases 17 to 32), D2 (Cases 33 to 48), and D3 (Cases 49 to 64) as well. Halving the number of sensors from 144 to 72 reduced the mean elapsed times by 1 order of magnitude, from a range between 1 and 20 s per run to 1–6 s per run (Figure 15a). Further reducing led to a maximum elapsed time not larger than 2 s, and so on.

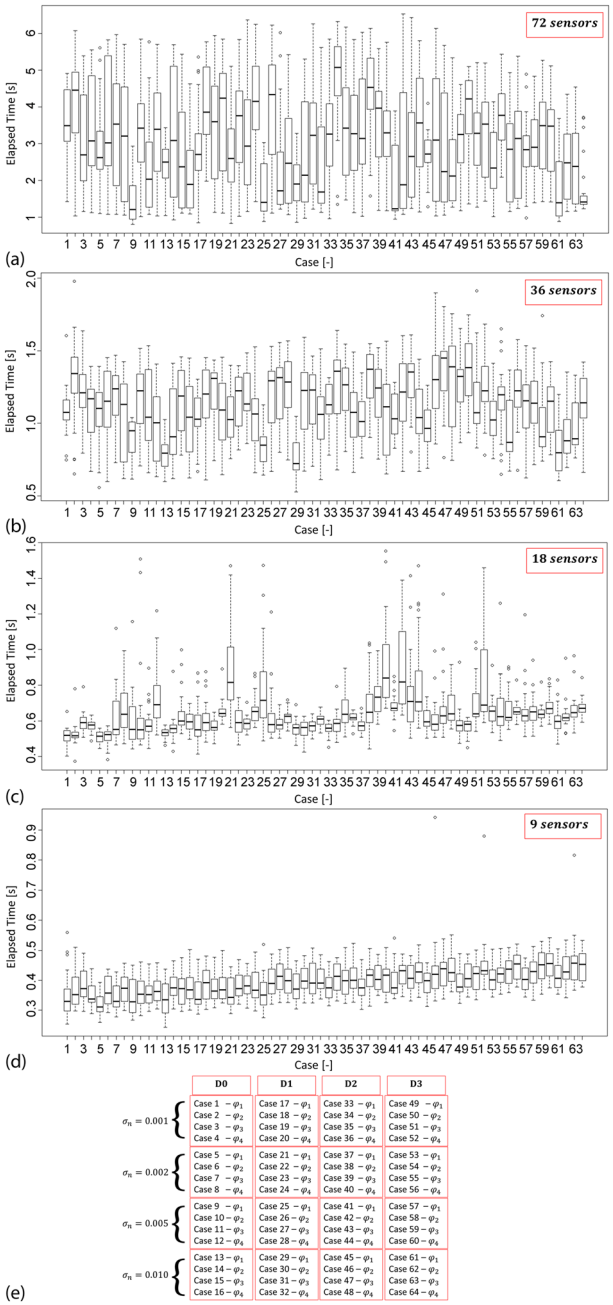

FIGURE 15 Box plot of the elapsed time (in seconds), with 72 (a), 36 (b), 18 (c), 9 (d) output channels, and legend (e)

It can be seen that, for all sensor setups, the fitting procedure becomes generally slower for increasing damage severity. Overall, the configuration with 18 sensors produced results consistent with the 144-sensors scenario, as it will be shown in the next paragraph, with a considerable gain in computational efficiency. On the other hand, the setup with only nine output channels, while even faster, returned less accurate results.

Very importantly, the erroneous branches tend to cluster around mode shapes' antinodes (i.e., the local maxima and minima). This is particularly evident for the UD Scenario D0 (Figures 11a and 12a), where the partitions occurred solely at the antinodes of the first and third mode shapes, respectively. The antinode closer to the beam mid-length is the one to be firstly localized. This point will be better addressed in the following subsection for experimental data. The strategy performed here was to compare the different mode shapes, to distinguish damage-related effects (which are present in all mode shapes at the same location) from mode shape-related ones (which affects differently the several vibrational modes). This is a common methodology that proved to be very effective in this investigation. The results according to the damage scenario and the noise level are reported in Figures 16 and 17 for 144 and 18 number of output channels (in the same order). It can be noticed that in this last case, the more influences by the antinodes of the second and third mode shapes; however, the damage is still noticeable. The reduced number of potential output even reduced the number of false bifurcations at the beam mid-length. On the other hand, considering only nine sensors produced some mixed results, making the actual damage location difficult to locate.

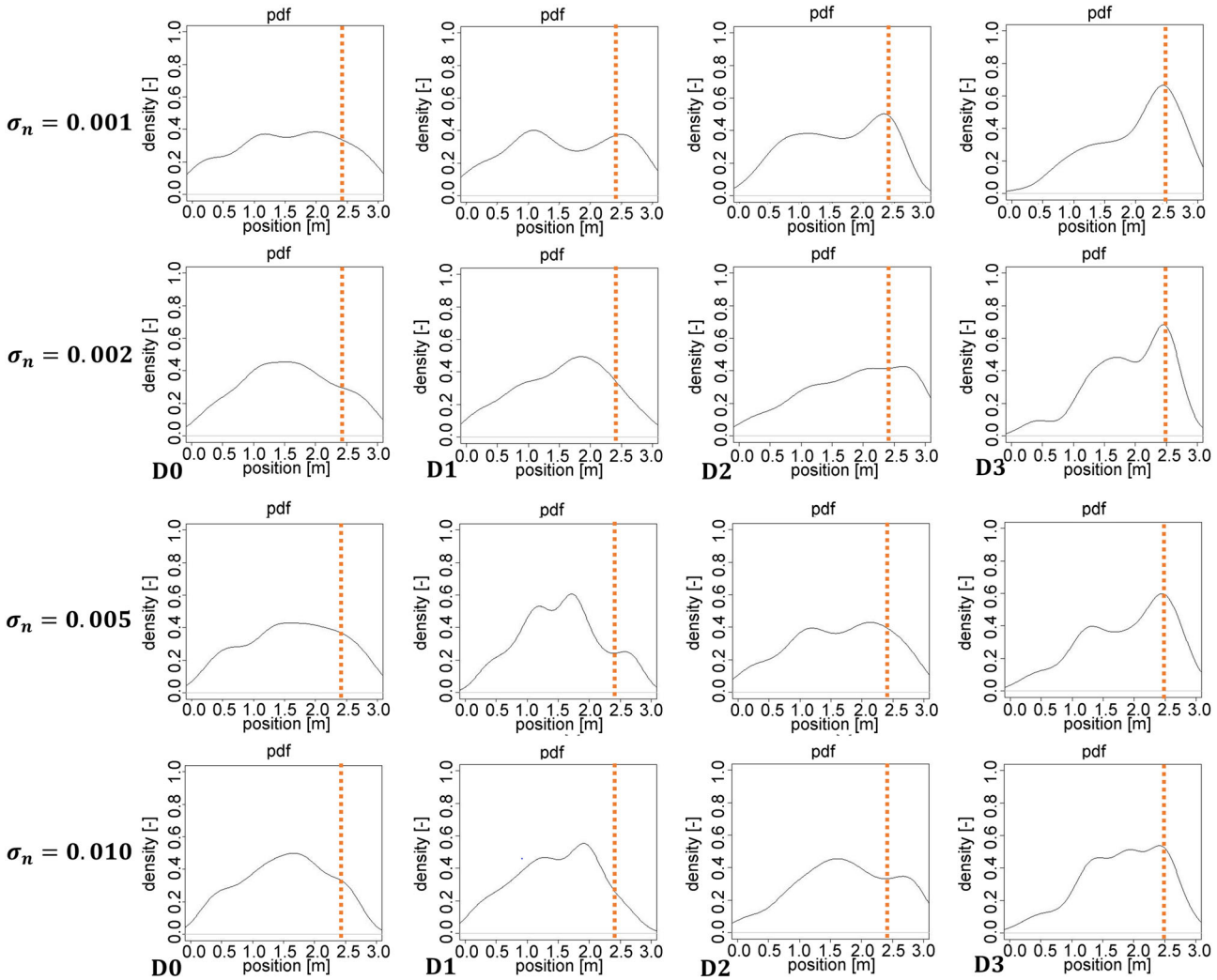

FIGURE 16 Probability density functions for all damage cases and noise levels; 144 output channels. The orange dotted lines represent the actual damage (2.468 m)

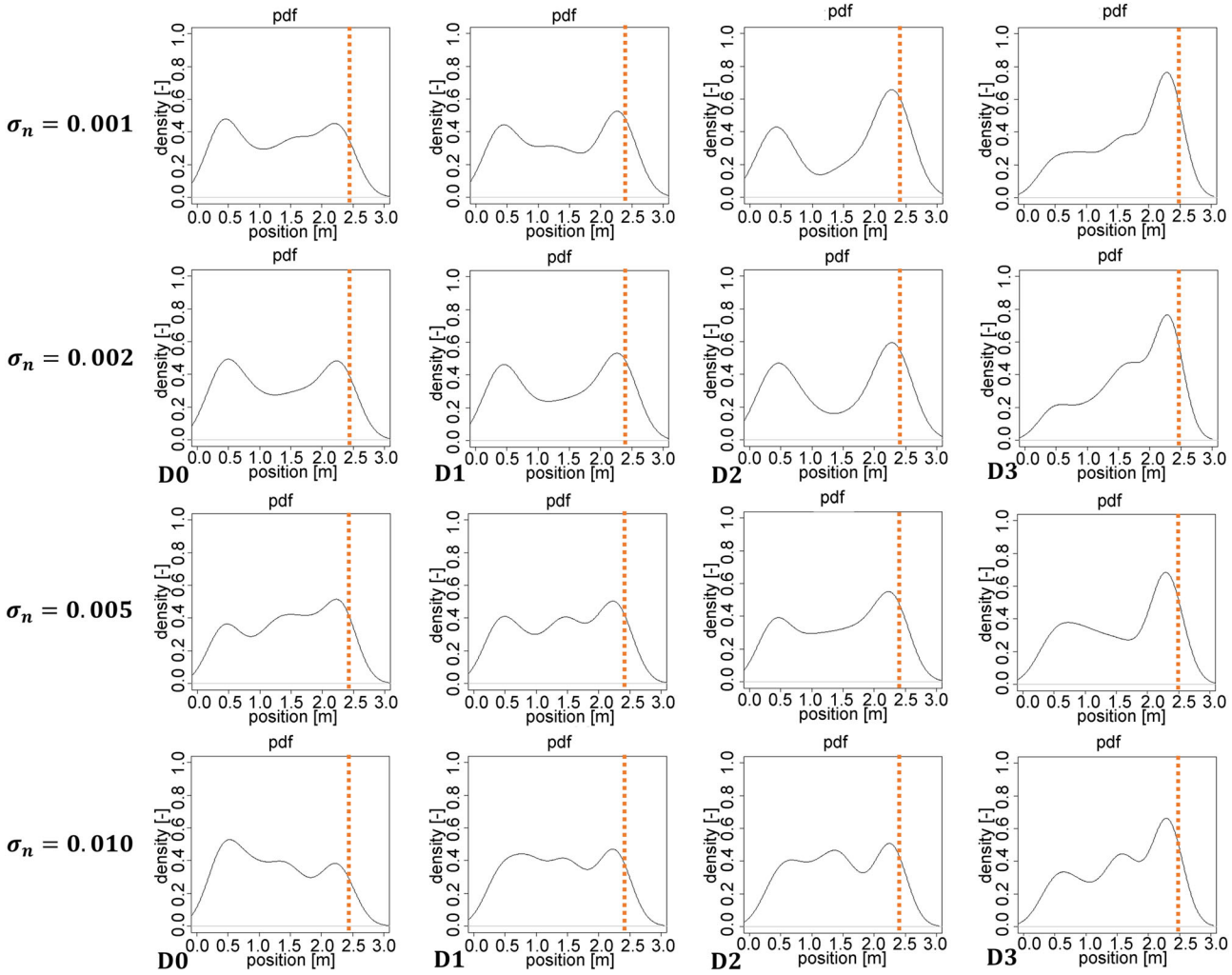

FIGURE 17 Probability density functions for all damage cases and noise levels; 18 output channels. The orange dotted lines represent the actual damage (2.468 m)

4.2 | TGP applied to experimental mode shapes

From the experience on numerically simulated data and considering the high level of measurement noise and the relatively low number of accelerometers available, it was chosen to inspect directly the mode shapes rather than deriving them once or twice. Indeed, it was found (for this specific set of data) that the negative effects of amplification on noise were much higher than the positive effects on damage-induced discontinuities.

The study was conducted on the first three mode shapes, computed for every damage condition following the configuration shown in Figure 4. Some of the data recorded were very poor, due to clipping. In this case, the signals were properly truncated and the part of signals saturated was discarded. Due to high measurement noise, some cases presented very deep trees, with many bifurcations. To overcome this issue, it was decided to take into account only the first branch, as done for numerical simulations. The algorithm was re-run 100 times per damage case and per mode shape, to validate the results statistically.

Some results are here reported in Figures 18–20 for increasing damage level and commented as an example; all discussions can be extended to similar cases. The portraited regressions and decision trees are used only to visualize the TGP output and are not to be intended as representative of the most common ramifications for their respective modes.

Figure 18 presents the first three modes for D1. The pointwise fitting of the TGP function (in solid red) was accurate in most of the re-runs inspected. The damage-induced local change in the mode shape is particularly marked in the first eigenshape. As it can be seen, the algorithm tends to branch erroneously at the extrema (local maxima and minima) of

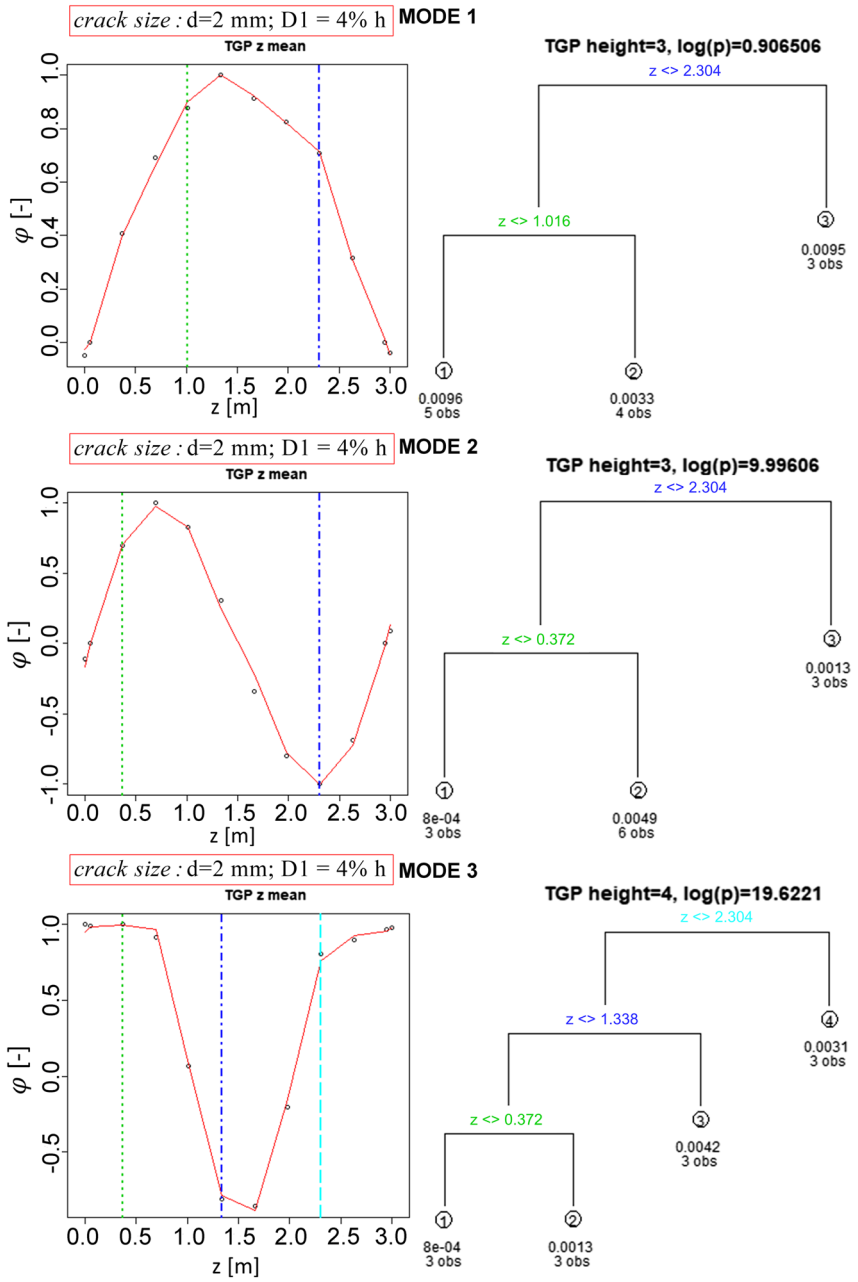

FIGURE 18 TGP regressions (solid red lines) over experimental data (black circles) for damage condition D1; dashed lines highlight the branching points at the boundary between subsequent GPs. Right: the corresponding hierarchical dendrogram of GP fittings. Branching points are colored accordingly to their corresponding dashed lines

the mode shapes, due to the shape functions inverting their trends. However, in the three examples reported, the first branch was always the one closer to the target (damaged) cross section. The same considerations apply to Figure 20. Conversely, Figure 19 reports for the first and second mode two examples of first branching happening at discontinuities unrelated to damage.

To mitigate the deleterious effects of spurious branching, it is possible to combine the results of the three mode shapes, as their nodes and antinodes differ; ideally, partitions unrelated to damage would cancel out. This is exactly what was achieved by multiplying the pdfs of the three modes for each damage case, as reported in Figure 21. The peak in the distribution of the resulting pdf corresponding to the damaged position is noticeably more marked than for the single modes taken individually. On the other hand, the effects of the increasing level of damage did not cause any major increase in the method accuracy.

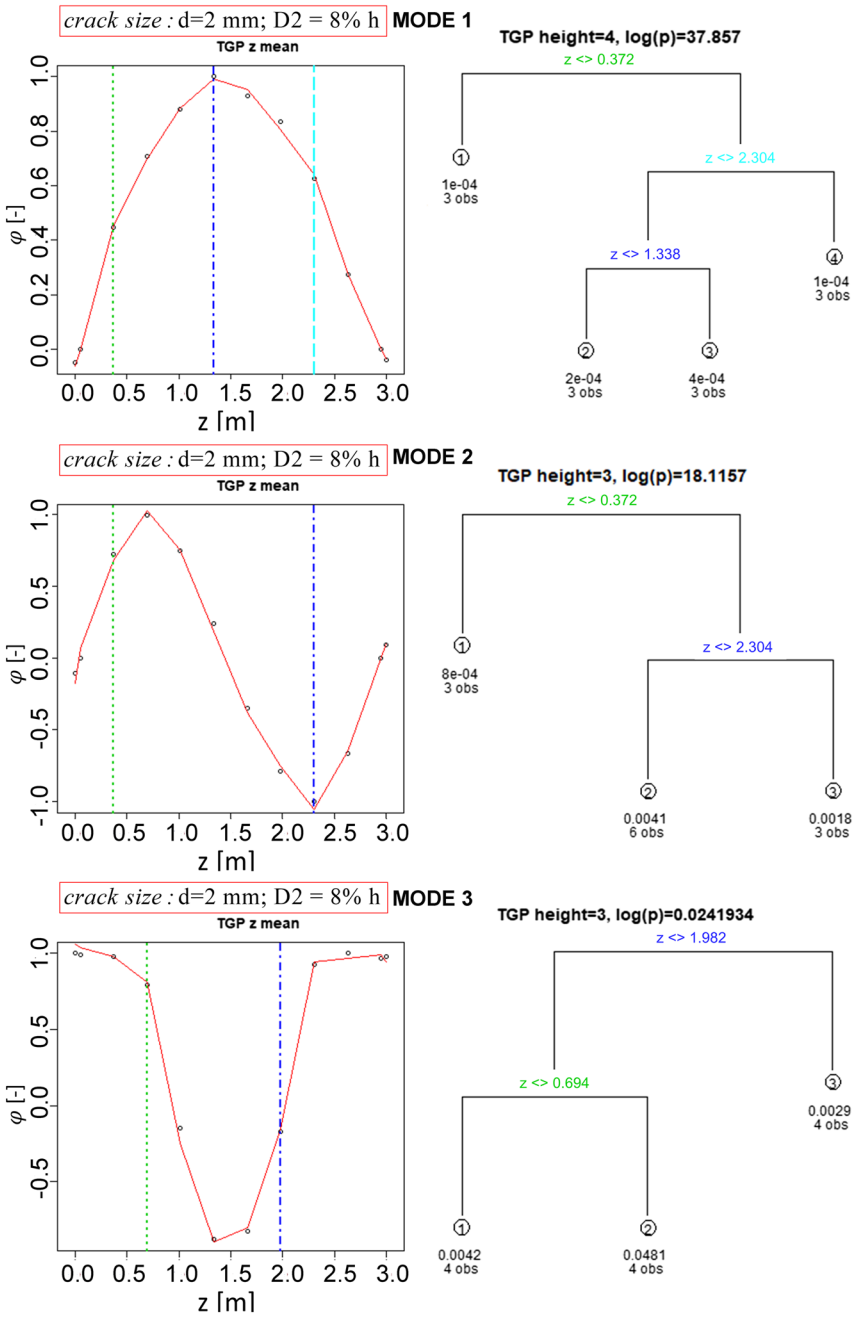

FIGURE 19 Left: TGP regressions (solid red lines) over experimental data (black circles) for damage condition D2. Right: the corresponding hierarchical dendrogram of GP fittings. Branching points are colored accordingly to their corresponding dashed lines

4.3 | Comparison with other established techniques

To further validate the proposed approach, its performances have been compared against the modal curvature[10] and modal flexibility methods,[55] which are widely considered the two of the most common procedures for mode shape-based damage localisation.[56]

The principles behind these two approaches are straightforward. In the first case, for a beam with constant flexural rigidity EI along all cross sections and subject to a bending moment $M(z)$, the curvature along the direction of its main axis can be defined as $\kappa(z) = M(z)/EI$. Therefore, $\kappa(z)$ is equivalent to the second spatial derivative of the corresponding mode shape $\varphi(z)$. Thus, $\kappa(z)$ can be easily defined by numerically deriving twice the estimated modal coordinates. The rationale is that the local reduction of stiffness associated with the presence of damage induces an increase in curvature.

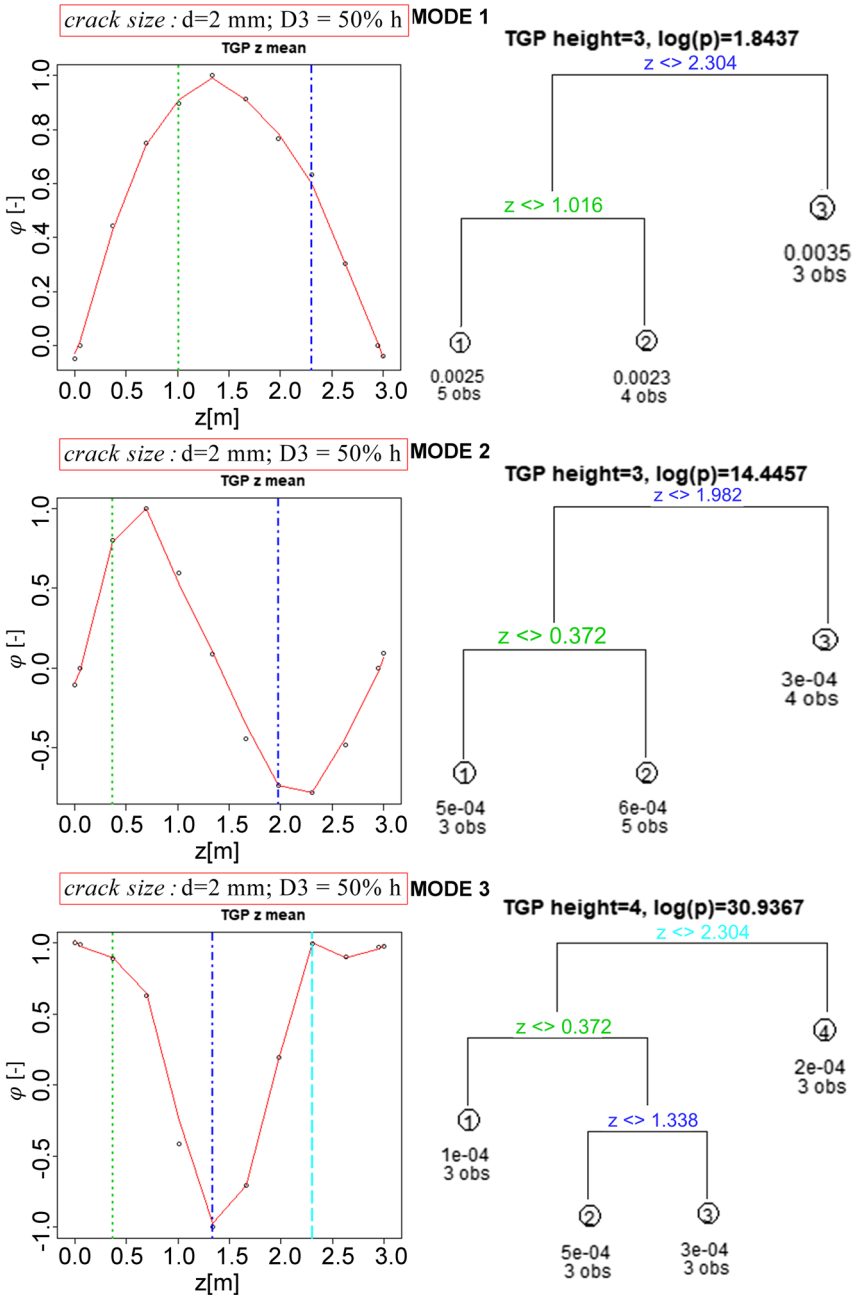

FIGURE 20 Left: TGP regressions (solid red lines) over experimental data (black circles) for damage condition D3. Right: the corresponding hierarchical dendrogram of GP fittings. Branching points are colored accordingly to their corresponding dashed lines

The criterion is to compare the absolute difference between the damaged and UD mode shapes, that is to say, $\Delta_\kappa = |\kappa_D(z) - \kappa_{UD}(z)|$.

Regarding the second classic technique, the structural flexibility matrix represents the inverse of the static stiffness matrix, that is, $\boldsymbol{F} = \boldsymbol{K}^{-1}$. This can be approximated as $\boldsymbol{F} \approx \boldsymbol{\Phi} \cdot \boldsymbol{1/\Omega^2}\ \boldsymbol{\Phi}^T$, where $\boldsymbol{\Phi} = \{\boldsymbol{\varphi_1}, \boldsymbol{\varphi_2}, \ldots, \boldsymbol{\varphi_N}\}$ is the matrix of the N mass-normalized, ordered mode shapes, $\boldsymbol{\Phi}^T$ its transpose, and $\boldsymbol{1/\Omega^2}$ is a diagonal matrix made up by the reciprocal of the square of the system's natural frequencies (expressed in radians). Thus, the flexibility depends on both the system's eigenvalues and eigenvectors. The approximation is due to the truncation to a finite number of modes of the continuous structure; however, the contribution of each mode to the total flexibility decreases rapidly as the corresponding natural frequency increases; thus, it is reasonable to consider only a subset of lower modes.[55] Note that, differently from the rest of this paper, the mode shapes in $\boldsymbol{\varphi}$ must be normalized with respect to the system mass rather than the maximum displacement. This is necessary to enforce that the flexibility of each component is properly defined (and thus

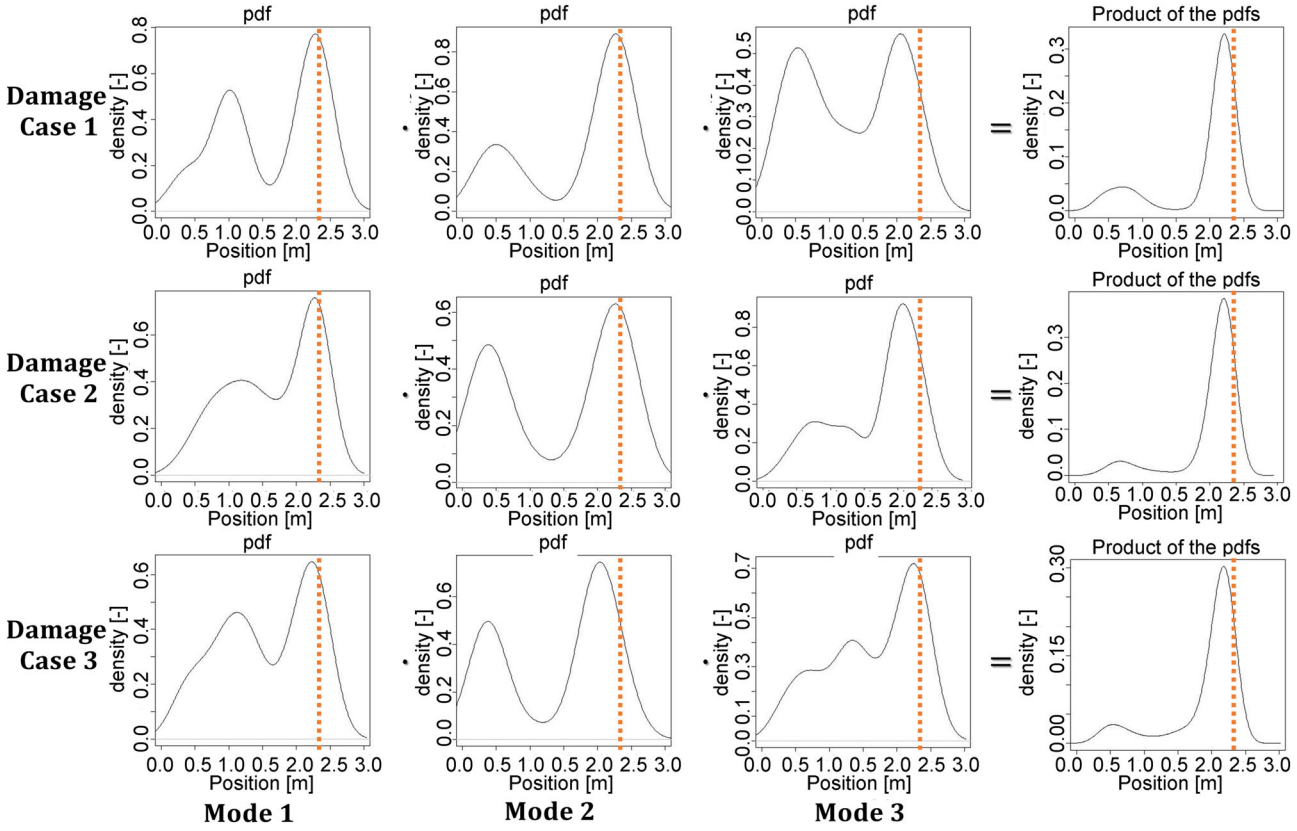

FIGURE 21 Probability density functions for the three damage cases considered (D1–D3). Illustrated separately on the three left columns and multiplied together on the last right column. The orange dotted lines represent the sensor closest to the actual damage (2.304 and 2.468 m, respectively)

comparable). While this can be simply achieved for a simpler structure like the beam investigated here, this technical issue represents a limitation for more complex scenarios, if a supporting FE model is not available.[55] As for the modal curvature, the concept is that the occurrence of damage decreases locally the structural stiffness, which is the inverse of the structural flexibility, and the differences between a given damaged case and the UD baseline are contained in the matrix $\Delta_{\mathbf{F}} = \boldsymbol{F_D} - \boldsymbol{F_{UD}}$.

The matrix $\Delta_{\mathbf{F}}$ can be utilized in different manners. Doebling and Farrar[57] suggested considering the diagonal entries in $\Delta_{\mathbf{F}}$, while Pandey and Biswas[55] considered the maximum absolute value among all the elements in the $i = 1, \ldots I$ rows of the corresponding jth column of $\Delta_{\mathbf{F}}$, that is to say, $\delta_j = \max_i(|\Delta_{\mathrm{F},ij}|)$. Both methods have been tested here.

By comparing the results of Figures 21–23, it can be seen that the described procedure better highlights the damage location. In particular, the damage-induced local increase in the modal curvature did not perform well in the case of interest. Deriving (twice) the data emphasizes the effects of both the damage and the measurement noise; for very noisy data like the ones investigated here, the negative side effects of the amplified noise overcome the potential benefits. Similarly, the damage-induced local increase in the modal flexibility did produce few appreciable variations; the local peak (more visible considering $\mathrm{diag}(\Delta_{\mathbf{F}})$) is not very prominent and lower than the global maximum at mid-span. This can be due to the relatively small damage, which caused minimal variation to the structural flexibility, and the few output channels. The few available modes may also have been not enough. For instance, for a real-life multi-span bridge deck, Catbas et al. suggested using at least the first nine modes.[58] Thus, both the classic procedures do not suit well very noisy data as the one analyzed here.

From a conceptual standpoint, both the modal curvature and the modal flexibility procedures rely on the comparison with the UD baseline, which cannot be available in real-life situations; this is not strictly necessary for the TGP algorithm described here. On the one hand, the TGP regression is undoubtedly more computationally demanding than numerical integration. On the other hand, the proposed algorithm uses several mode shapes at once to discard damage-unrelated effects, differently from the other techniques, and returns automatically the defined

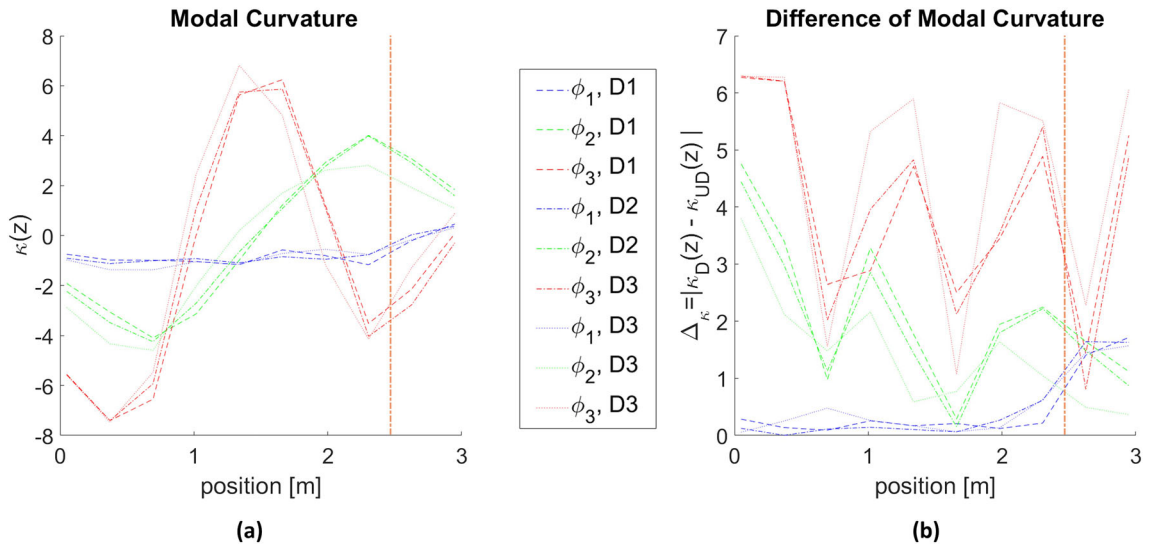

FIGURE 22 (a) Experimental modal curvatures. (b) Results of the modal curvature procedure. The first three modes are colored in blue, green, and red (in this order). D1: dashed line; D2: dashed-dotted line; D3: dotted line. The vertical orange line indicates the actual damage location

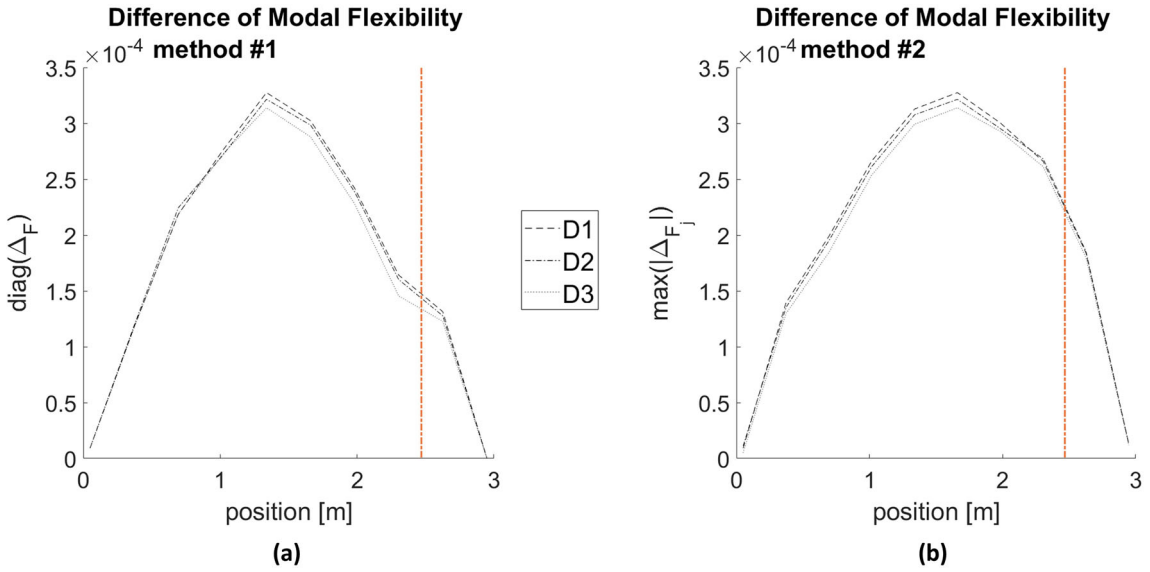

FIGURE 23 Results of the modal flexibility procedure: (a) Doebling and Farrar procedure; (b) Pandey and Biswas procedure. D1: dashed line; D2: dashed-dotted line; D3: dotted line. The vertical orange line indicates the actual damage location

partitions, while the partitioning needs to be performed "by eye" with the other techniques, according to the user's subjective opinion.

It must be said that there are no conceptual nor technical limitations to apply the proposed TGP-based procedure on modal curvature or rotations rather than on mode shapes. That is to say, the two methods can be easily combined. For less noisy measurements, where the differentiation can lead to an increased sensibility, this can be beneficial for a more reliable localization. Figure 24 reports a simple example, for the cantilevered beam described in Figure 1 in an ideally noise-free condition (a second crack has been added at 60 cm from the left end; the severity of both damages has been reduced to a 20% decrease of Young's modulus). As can be seen, in optimal conditions, the beneficiary effects of numerically deriving allow to identify and locate damages otherwise not detectable in the raw data.

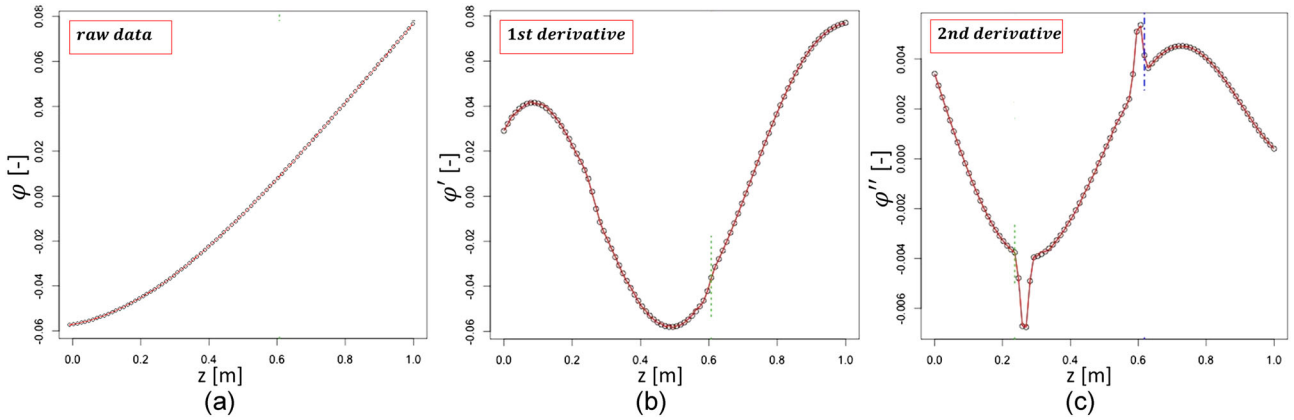

FIGURE 24 An example of TGP applied to (a) a raw mode shape, (b) its first spatial derivative (modal rotation), partitioned one time in correspondence of the second damaged element, and (c) its second spatial derivative (modal curvature), partitioned twice in correspondence of both damaged elements

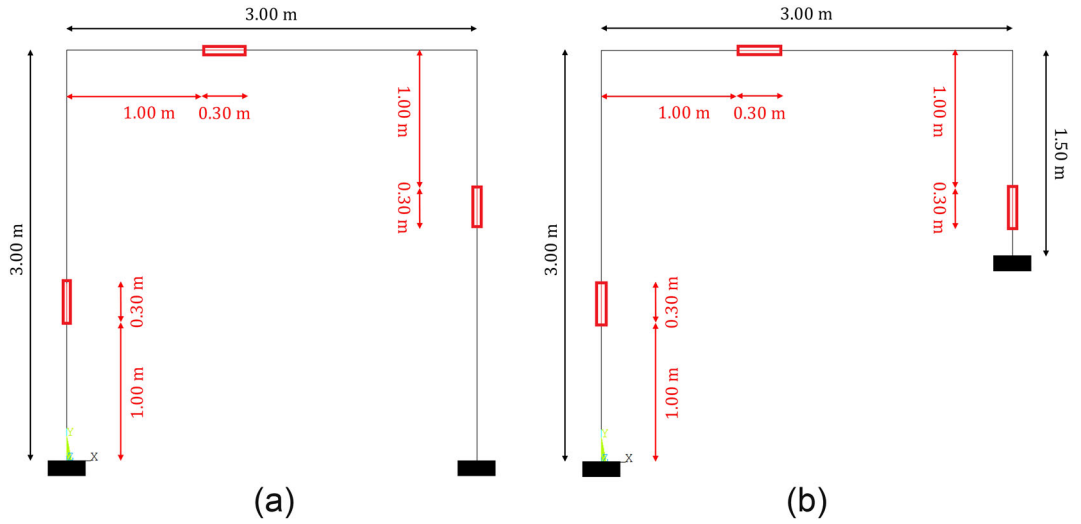

FIGURE 25 The two portals considered: (a) P1 (symmetric geometry) and (b) P2 (asymmetric geometry)

5 | VALIDATION FOR MULTIPLE DAMAGE LOCATIONS ON A FRAME STRUCTURE

To conclude this investigation, the TGP algorithm has been tested on two-dimensional structures with multiple damages. Specifically, the two single-story, single-span, unbraced plane frames depicted in Figure 25a,b have been considered, with the corresponding damage pattern portrayed there.

In both the first (P1) and the second case (P2), three damages were inserted in the left column, the horizontal beam, and the right column always at 1 m from the first end (moving from the bottom left clockwise). Similarly to the first numerical example, the damage was modeled in the FE models as a 50% reduction of the stiffness of the highlighted elements (for all the cross section and a length of the single element equal to 30 cm). The same material and cross section as for the GFRP beam have been considered. For consistency with the other numerical examples, the first four mode shapes have been utilized. A noise level of $\sigma_n = 0.005$ was artificially added. It was considered to have one output channel, orthogonal to the structure, at any 5 cm. The results are portrayed in Figure 26. For brevity, only the first and the last (fourth) mode shapes are reported, respectively for P1 and P2, plus the final pdfs. As can be seen, the method captures well the multiple damage positions on the three segments of the planar frame.

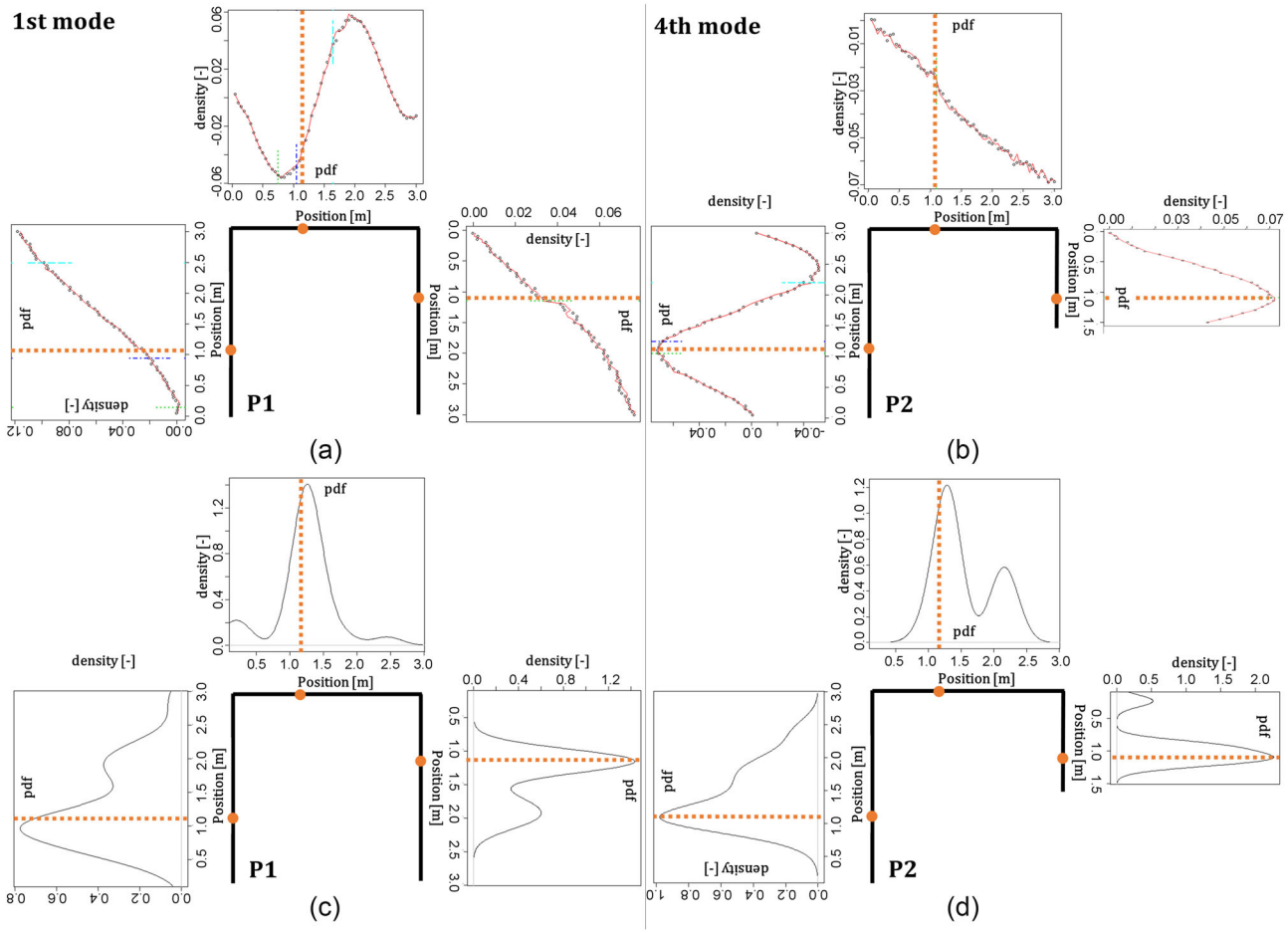

FIGURE 26 Top row: results for (a) the first mode shape of P1 and (b) the fourth mode shape of P2. Bottom row: probability density functions for the two cases, multiplied together considering the first four vibrational modes, (c) P1 and (d) P2. The orange dotted lines represent the sensors closest to the actual damage locations

6 | CONCLUSIONS

Only a very few works reported in the scientific literature deals with the damage localization in pultruded composites. In this context, a TGP approach has been presented here. In the GP regression, a covariance kernel, which characterizes the smoothness of the structure being modeled, is used. GPs are statistically based (Bayesian) and are therefore able to automatically return the confidence interval for predictions at any location. Combining them with Bayesian CARTs, pointwise regression allows to detect discontinuities at the edges between neighboring branches. That is known as TGP regression and partitioning, and it was used here as a mean of localization for incongruences in numerical and experimental perturbed mode shapes. The method has been initially proved on numerically simulated cases for well-defined slots. A study of the effects of measurement noise and damage severity has been performed as well. The method has then be applied to experimental data coming from a saw-cut pultruded GFRP beam for increasing levels of damage.

The GP regression is notoriously highly expensive, computationally speaking. For n points, n^3 operations are needed. Combining it with the thousands of steps required by the MCMC process, the whole process is not computationally efficient. Yet it has the great advantage of requiring minimal assumptions on the data to be fitted, thus granting a very high generalization capability.

In both numerical and experimental studies, the damage was clearly identified as disturbances in the eigenshapes, which are generally related to damage local effect on modal data. The main aim was to test TGP capabilities to automatically locate the discontinuities in the mode shape along the beam main axis. These discrepancies in the mode shapes were found in all the normal modes investigated and localized in a certain portion of the beam. These points are therefore the most likely candidates as the main location of damages.

TGPs correctly located the abovementioned discontinuities in the experimental mode shapes with an acceptable level of accuracy for the first modes. The procedure can be greatly improved if only the first (most discriminative) branch is considered. However, both numerical and experimental results show that the method is extremely sensitive to overfitting, which results in branching at antinodes (local minima and maxima of the shape function). The inconvenience can be easily bypassed by comparing (at least) two mode shapes from the same input as done here by multiplying the obtained pdfs of the first four vibrational modes.

Overall, the procedure described in this paper returned more evidently the actual location of damage in comparison to other common alternatives (the modal curvature and the modal flexibility techniques). It was also proved able to detect multiple damages in two-dimensional structures (specifically, on a frame portal).

The method proved to be sensitive to measurement noise. While despicable, this is a very well known issue for most of the damage localization techniques. Numerical results seem to point out that the most detrimental effects happen for high noise levels, but the trend is not monotonical. Noise-free data perform obviously better than highly noisy ones, yet a small amount of noise apparently helps the TGP routine to avoid overfitting and produces much less erroneous branching than the same numerical data with a lower level of artificially added disturbance. As expected, very high noise overwhelms interesting effects. Future works will also include a better way to deal with all these technical problems.

ACKNOWLEDGMENTS

The authors wish to thank Università Iuav di Venezia, Politecnico di Torino, and Cranfield University for this joint collaboration.

AUTHOR CONTRIBUTIONS

G. Boscato: conceptualization; methodology; validation; formal analysis; resources; writing—original draft preparation; visualization. M. Civera: conceptualization; methodology; software; formal analysis; resources; writing—original draft preparation; visualization. L. Zanotti Fragonara: conceptualization; methodology; formal analysis; resources; writing—review and editing; visualization.

ORCID

Giosuè Boscato https://orcid.org/0000-0001-6537-3084
Marco Civera https://orcid.org/0000-0003-0414-7440
Luca Zanotti Fragonara https://orcid.org/0000-0001-6269-5280

REFERENCES

1. Barbero EJ. *Introduction to Composite Materials Design*. 1sted. Philadelphia, PA: Taylor and Francis; 1999.
2. Anonymous. *Strongwell Design Manual*. Bristol, VA: Strongwell Composites Inc (www.strongwell.com).
3. Anonymous. *The Pultrex Pultrusion Design Manual* (Imperial version) Vol. 4 Rev. 6. Alum Bank, PA: Creative Pultrusion Inc. (www.creativepultrusions.com/library.html).
4. Farrar CR, Worden K. *Structural Health Monitoring: A Machine Learning Perspective*. New York: Wiley; 2013.
5. Yoon MK, Heider D, Gillespie JW Jr, Ratcliffe CP, Crane RM. Local damage detection with the global fitting method, part A: using mode shape data in notched beams. *J Nondestruct Eval*. 2009;28(2):63-74.
6. Ferraris M, Civera M, Ceravolo R, Surace C, Betti R. *Using Enhanced Cepstral Analysis for Structural Health Monitoring*. Singapore: Springer; 2020:150-165 https://doi.org/10.1007/978-981-13-8331-1_11
7. Civera M, Ferraris M, Ceravolo R, Surace C, Betti R. The Teager–Kaiser energy cepstral coefficients as an effective structural health monitoring tool. *Appl Sci*. 2019;9(23):5064. https://doi.org/10.3390/app9235064
8. Crema L, Castellani A, Coppotelli G. Damage localization in composite materials structures by using eigenvalue measurements. *Mater Des Technol*, ASME. 1995;PD-7:201-205.
9. Messina A, Williams E, Contursi T. Structural damage detection by a sensitivity and statistical-based method. *J Sound Vib*. 1998;216(5):791-808.
10. Pandey A, Biswas M, Samman M. Damage detection from changes in curvature mode shapes. *J Sound Vib*. 1991;145(2):321-332.
11. Wahab M, Roeck G. Damage detection in bridges using modal curvatures: application to a real damage scenario. *J Sound Vib*. 1999;226(2):217-235.
12. Kim JT, Ryu YS, Cho HM, Stubbs N. Damage identification in beam-type structures: frequency-based method vs mode-shape-based method. *Eng Struct*. 2003;25(1):57-67.
13. Yoon MK, Heider D, Gillespie JW Jr, Ratcliffe CP, Crane RM. Local damage detection using the two-dimensional gapped smoothing method. *J Sound Vib*. 2005;279(1–2):119-139.

14. Ratcliffe CP. Damage detection using a modified Laplacian operator on mode shape data. *J Sound Vib*. 1997;204(3):505-517.
15. Ratcliffe CP. A frequency and curvature based experimental method for locating damage in structures. *J Vib Acoust*. 2000;122(3): 324-329.
16. Civera M, Zanotti Fragonara L, Surace C. A novel approach to damage localisation based on bispectral analysis and neural network. *Smart Struct Syst*. 20(6):669-682.
17. Hensman J, Surace C, Gherlone M. Detecting mode-shape discontinuities without differentiating—examining a Gaussian process approach. In *Proceedings of 9th International Conference in Damage Assessment (DAMAS 2011)*, Oxford (2011).
18. Rasmussen CE, Williams C. *Gaussian Processes for Machine Learning*. New York: The MIT Press; 2006.
19. Gramacy RB. Bayesian Treed Gaussian Process models (Doctoral dissertation, University of California, Santa Cruz), Chap 5, 2005.
20. Gramacy RB, Lee HKH. Bayesian treed Gaussian process models with an application to computer modeling. *J Am Stat Assoc*. 2008; 103(483):1119-1130.
21. Becker W, Worden K, Rowson J. Bayesian sensitivity analysis of bifurcating nonlinear models. *Mech Syst Signal Process*. 2013;34(1–2): 57-75.
22. Baldacchino T, Cross EJ, Worden K, Rowson J. Variational Bayesian mixture of experts models and sensitivity analysis for nonlinear dynamical systems. *Mech Syst Signal Process*. 2016;(66–67):178-200.
23. Worden K, Cross EJ, Brownjohn JMW. Switching response surface models for structural health monitoring of bridges. In: Koziel S, Leifsson L, eds. *Surrogate-Based Modeling and Optimization*. New York, NY: Springer; 2013.
24. Worden K, Cross EJ. On switching response surface models, with applications to the structural health monitoring of bridges. *Mech Syst Signal Process*. 2018;98:139-156. https://doi.org/10.1016/j.ymssp.2017.04.022
25. Zhang T, Barthorpe R, Worden K. A simplified treed gaussian process approach to the modelling of bridge data for structural health monitoring. *Struct Health Monit*. 2017;1–10. https://doi.org/10.12783/shm2017/13910
26. Zhang T, Barthorpe R, Worden K. On Treed Gaussian Processes and piecewise-linear NARX modelling. *Mech Syst Signal Process*. 2020; 144:106877.
27. Civera M, Boscato G, Zanotti Fragonara L. Treed Gaussian Process for manufacturing imperfection identification of pultruded GFRP thin-walled profile. *Compos Struct*. (in publication) 2020;254:112882.
28. Civera M, Surace C, Worden K. Detection of cracks in beams using Treed Gaussian Processes. In: Niezrecki C, ed. *Structural Health Monitoring & Damage Detection*. Conference Proceedings of the Society for Experimental Mechanics Series. Vol. 7. Cham: Springer; 2017.
29. Corrado N, Durrande N, Gherlone M, Hensman J, Mattone M, Surace C. Single and multiple crack localization in beam-like structures using a Gaussian process regression approach. *J Vib Control*. 2019;24(18):4160-4175.
30. Gauthier JF, Whalen TM, Liu J. Experimental validation of the higher-order derivative discontinuity method for damage identification. *Struct Control Health Monit*. 2008;15(2):143-161.
31. Casciati S, Elia L. Damage localization in a cable-stayed bridge via bio-inspired metaheuristic tools. *Struct Control Health Monit*. 2017; 24(5):e1922.
32. An Y, Błachowski B, Zhong Y, Hołobut P, Ou J. Rank-revealing QR decomposition applied to damage localization in truss structures. *Struct Control Health Monit*. 2017;24(2):e1849.
33. Stojić D, Nestorović T, Marković N, Marjanović M. Experimental and numerical research on damage localization in plate-like concrete structures using hybrid approach. *Struct Control Health Monit*. 2018;25(9):e2214.
34. Chipman HA, George EI, McCulloch RE. Bayesian cart model search. *J Am Stat Assoc*. 1998;93(443):935-948.
35. Geman S, Geman D. Stochastic relaxation, Gibbs distributions, and the Bayesian restoration of images. *IEEE Trans Pattern Anal Mach Intell*. 1984;6(6):721-741. https://doi.org/10.1109/TPAMI.1984.4767596
36. Gramacy RB. *tgp:* An R package for Bayesian nonstationary, semiparametric nonlinear regression and design by treed Gaussian process models. *J Stat Softw*. 2007;19:1–47. https://doi.org/10.18637/jss.v019.i09
37. Cohn DA. Neural network exploration using optimal experimental design. *Neural Netw*. 1996;9(6):1071-1083.
38. Lee HKH, Gramacy RB. Adaptive design and analysis of supercomputer experiments. *Dent Tech*. 2009;51(2):130-145. https://doi.org/10.1198/TECH.2009.0015
39. MacKay DJC. Information-based objective functions for active data selection. *Neural Comput*. 1992;4(4):590-604.
40. Jones D, Schonlau. M, Welch WJ. Efficient global optimization of expensive black box functions. *J Glob Optim*. 1998;13(4):455-492.
41. Gramacy RB, Matthew Alan TM. Categorical inputs, sensitivity analysis, optimization and importance tempering with tgp version 2, an R package for Treed Gaussian Process models. *J Stat Softw*, Foundation for Open Access Statistics. 2010;33(i06):1–49.
42. Chipman HA, George EI, McCulloch RE. Bayesian Treed Models. *Mach Learn*. 2002;48(1–3):299-320. https://doi.org/10.1023/A:1013916107446
43. Qian GL, Gu SN, Jiang JS. The dynamic behaviour and crack detection of a beamwith crack. *J Sound Vib*. 1990;138(10):233-243.
44. Anonymous. Fiberline design manual for structural profiles in composite materials. Fiberline Composites A/S, Kolding, Denmark, 1st Ed. 1995, updated 2nd Edition 2001.
45. Anonymous. In: Clarke JL, E & FN SPON, eds. *EUROCOMP Design Code and Handbook, Structural Design of Polymer Composites*; 1996.
46. CEN TC250 WG4L, Ascione L, Caron JF, Godonou P, van Ijselmuijden K, Knippers J, Mottram JT, Oppe M, Gantriis Sorensen M, Taby J, Tromp L Editors: Ascione L, Gutierrez E, Dimova S, Pinto A, Denton S. Prospect for new guidance in the design of FRP, support to the implementation and further development of the Eurocodes, JRC Science and Policy Report JRC99714, EUR 27666 EN, European

Union, Luxembourg, (2016), p 171. ISBN 978–92-79-https://amstat.tandfonline.com/doi/abs/10.1198/016214508000000689?casa_token=dpx4L8VN2XEAAAAA:8jh893Bmyc0CDTkeJxcLS55_mEhAOypKcWhREMlDh9tp-a6dklnQQQEMKP3BCWbVHin6nqv_lrPijw225-1 doi:10.2788/22306.
47. UNI EN 13706-2:2003. Reinforced plastics composites. Specifications for pultruded profiles. Method of test and general requirements.
48. Civera M, Zanotti Fragonara L, Surace C. An experimental study of the feasibility of phase-based video magnification for damage detection and localisation in operational deflection shapes. *Strain*. 2020;56(1):e12336. https://doi.org/10.1111/str.12336
49. Juang JN, Pappa R. An eigensystem realization algorithm for modal parameter identification and model reduction. *J Guid Control Dynam*. 1985;8(5):620-627.
50. Ewins DJ. *Modal testing*. Research Studies Press Ltd; 2000.
51. Cecchi A, Di Marco R. Glass fiber reinforced polymer pultruded members: constitutive model and stability analysis. *J Eng Mech* ASCE. 2004;130(8) August 1,:961-970.
52. Barbero EJ. *Finite Element Analysis of Composite Materials*, Taylor & Francis Group, 2008.
53. Pugno N, Surace C, Ruotolo R. Evaluation of the non-linear dynamic response to harmonic excitation of a beam with several breathing cracks. *J Sound Vib*. 2000;235(5):749-762.
54. Civera M, Zanotti Fragonara L, Surace C. Nonlinear dynamics of cracked, cantilevered beam-like structures undergoing large deflections. In 2019 IEEE 5th International Workshop on Metrology for AeroSpace (MetroAeroSpace) (pp. 193–202). IEEE
55. Pandey AK, Biswas M. Damage detection in structures using changes in flexibility. *J Sound Vib*. 1994;169(1):3-17.
56. Dawari VB, Vesmawala GR. Modal curvature and modal flexibility methods for honeycomb damage identification in reinforced concrete beams. *Procedia Eng*. 2013;51:119-124.
57. Doebling SW, Farrar CR. *Computation of Structural Flexibility for Bridge Health Monitoring Using Ambient Modal Data*. 1996.
58. Catbas FN, Brown DL, Aktan AE. Use of modal flexibility for damage detection and condition assessment: case studies and demonstrations on large structures. *J Struct Eng*. 2006;132(11):1699-1712.

How to cite this article: Boscato G, Civera M, Zanotti Fragonara L. Recursive partitioning and Gaussian Process Regression for the detection and localization of damages in pultruded Glass Fiber Reinforced Polymer material. *Struct Control Health Monit*. 2021;e2805. https://doi.org/10.1002/stc.2805